Catalysis
Science &
Technology

ROYAL SOCIETY
OF **CHEMISTRY**

REVIEW

View Article Online
View Journal

Check for updates

Cite this: DOI: 10.1039/d5cy01360g

Advancements in nitrous oxide abatement: a review of direct catalytic decomposition and selective catalytic reduction

Han Chau,†[a] Sarah Stofik,†[b] Matthew N. Gordon,[c] Mark Mueller,[d] Rebecca Fushimi,[a] Dilpuneet S. Aidhy,[d] Matthew Craps,[c] Jochen Lauterbach *[b] and Dylan D. Rodene *[c]

Nitrous oxide (N_2O) emissions pose significant environmental and regulatory challenges, which necessitates a need for advancements in catalytic abatement methods. This review evaluates catalytic systems with insights for industrial applications, covering three catalyst types: supported metal catalysts (Rh/CeO_2, $Ru/\gamma\text{-}Al_2O_3$, Rh/Al_2O_3, and Pd/Al_2O_3), transition metal oxides (Co_3O_4, Mn_2O_3, CuO, and NiO), and ion-exchanged zeolites (Fe-, Co-, and Cu- on ZSM-5, BEA, SSZ-13, FER, and MOR). For direct decomposition reactions, the catalytic performance is influenced by the redox and oxygen desorption properties, as well as by the inclusion of promoters. For SCR applications, iron-based zeolites (*e.g.*, Fe-MFI, Fe-MOR, Fe-BEA, and Fe-SSZ-13) offer high activity, low cost, and low toxicity. Among the reductants, CO and hydrocarbons demonstrate superior efficiency when compared to H_2 and NH_3 for Fe-BEA zeolites. The presence of O_2 and H_2O was shown to inhibit both reaction pathways, while SO_2 can cause irreversible deactivation. For SCR, NO demonstrates competitive adsorption, which inhibits the reaction with CO and hydrocarbon reductants. Additionally, transient kinetic studies and density functional theory were highlighted in terms of how they inform reaction mechanisms. Furthermore, high-throughput experimentation and machine learning can be leveraged to overcome the current and future industrial shortcomings of N_2O abatement processes.

Received 13th November 2025,
Accepted 18th May 2026

DOI: 10.1039/d5cy01360g

rsc.li/catalysis

1 Introduction

Nitrous oxide (N_2O) is a detrimental pollutant that accounts for ~6.2% of the anthropogenic greenhouse gas emissions.[1] N_2O has an atmospheric lifetime of ~131 years, which leads to prolonged harmful effects on the environment (*i.e.*, contributing to ozone depletion). Fig. 1 summarizes the natural and anthropogenic sources of N_2O. While natural sources are the primary contributors of N_2O emissions, industrial processes have led to a rapid increase in the emissions (as shown in the inset of Fig. 1).[2–5] Consequently, abatement methodologies should be considered in processes that emit N_2O and treat NO_x emissions, such as adipic acid production and the industrial oxidation of ammonia (NH_3), which accounted for 76% of N_2O emissions from chemical industries in 2020 alone.[6,7] Emissions from industrial applications alone warrant the implementation of abatement strategies to address the continuously rising emissions.[8–16]

Among the various N_2O abatement approaches, direct catalytic decomposition and selective catalytic reduction (SCR) of N_2O have been extensively studied in the literature, are widely applied in industry, and serve as the primary focus of this review. Although several recent comprehensive reviews

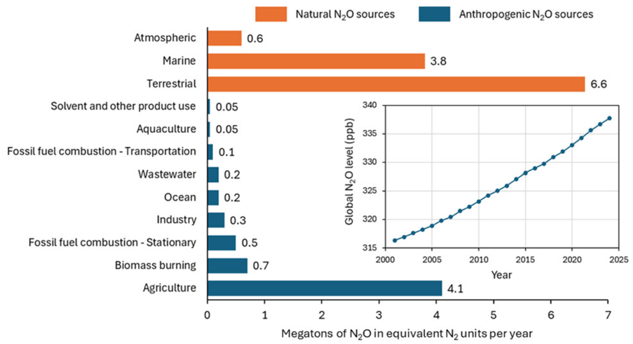

Fig. 1 Quantification of natural and anthropogenic sources of N_2O emissions by category with globally averaged atmospheric abundance over time (inset). Data from ref. 2 and 4.

---

[a] Catalysis and Transient Kinetics Group, Idaho National Laboratory, Idaho Falls, Idaho 83415, USA

[b] Department of Chemical Engineering, University of South Carolina, Columbia, SC 29208, USA. E-mail: lauteraj@cec.sc.edu

[c] Advanced Materials & Process Technologies Group, Savannah River National Laboratory, Aiken, SC 29808, USA. E-mail: Dylan.Rodene@srnl.doe.gov

[d] Department of Materials Science and Engineering, Clemson University, Clemson, SC 29634, USA

† These authors contributed equally.

have analyzed N_2O abatement strategies, this review uniquely emphasizes the most commonly used catalytic systems for both direct decomposition and SCR of N_2O.[8–13]

A systematic comparison of T_{50} values for the direct decomposition and SCR of N_2O, as reported in the literature, was performed based on the feed conditions provided. To enable further comparisons across the systems, gas hourly space velocity (GHSV), weight hourly space velocity (WHSV), and/or weight to volumetric flow (W/F) values were calculated (if not explicitly reported for each reference and the data was available). This standardization allows for the evaluation of catalyst performance under varying reaction conditions. Supported metals, metal oxides, and zeolites form the primary catalyst classes compared in this review, with reported or extracted T_{50} values contextualized based on their respective GHSV, WHSV, and/or W/F values reported herein. Additionally, emerging catalysts, such as single-atom catalysts and high-entropy oxides (HEOs), are discussed. This review also considers the use of both conventional and unconventional reductants, as well as the effects of impurity gases, in N_2O abatement processes. Studies on catalyst durability remain limited, regardless, oxide-based and zeolite-type catalysts stability will be discussed in sections 2.5 and 3.5.

Beyond catalyst performance evaluations, this review delves into key reaction mechanisms and considers insights gained at a molecular level from advanced tools such as density functional theory (DFT) and temporal analysis of products (TAP) studies. Furthermore, this review provides a forward-looking perspective on leveraging machine learning (ML) approaches and high-throughput experimentation (HTE) to accelerate catalyst discovery. These innovative methodologies have the potential to guide the development of novel catalysts, provide fundamental mechanistic insights, and enable rapid catalyst screening, to guide the field toward efficient industrial N_2O abatement.

1.1 Thermo-catalytic performance definitions

For N_2O abatement, a variety of metrics exist to analyze catalytic activity and track reaction performance. Conversion efficiency is used to track the reaction progress over a range of temperatures for a catalytic system and is reported as the fraction of reactants (*i.e.*, N_2O) that were converted to products. Gas chromatography (GC), Fourier-transform infrared spectroscopy (FTIR), and mass spectrometry (MS) are commonly used to quantify conversion efficiency for the gaseous analytes.

The T_{50} number (also known as the light-off temperature) is also commonly reported for N_2O abatement. The T_{50} number is the temperature at which conversion efficiency reaches 50% completion (*i.e.*, the center of an *S*-curve conversion *vs.* temperature plot), where a lower T_{50} number represents a more active catalyst system.

Conversion efficiency and T_{50} alone do not account for the intrinsic properties of the catalyst and are easily impacted by temperature, metal loading, and gas flow rate.[17] Therefore, the additional knowledge of the GHSV allows for a better comparison between catalysts by accounting for the volumetric flow rate of reactants to the catalyst bed with respect to the volume of the catalyst utilized. Similarly, the WHSV is also commonly reported and expresses the mass flow rate of reactants to the catalyst bed with respect to the weight of the catalyst. The ratio of the amount of catalyst to the flow rate (W/F) is also commonly reported. The GHSV, WHSV, and W/F help to provide additional insights when comparing reported catalytic conversion efficiencies and T_{50} values of a system (*e.g.*, larger flowrates with lower masses of catalyst will result in a larger space velocity, resulting in a lower apparent activity).

The T_{50} numbers at specified flow conditions will be the main metric reported to compare N_2O abatement catalysts. Furthermore, turnover frequency is not reported herein, due to difficulties in determining the number of active sites, as well as a lack of reporting in literature.[18]

1.2 Overview and application-based considerations

The use of direct decomposition reaction schemes *versus* the SCR of N_2O presents distinct challenges and considerations. Direct decomposition enables the abatement of N_2O into N_2 and O_2 without additional reactants, whereas SCR adds additional reductants such as CO, hydrocarbons, NH_3, or H_2 to aid in decomposition. An overview of the performance of various catalyst systems (supported metals, metal oxides, and zeolites) is shown in Fig. 2, highlighting T_{50} values for direct decomposition (Fig. 2B) and SCR of N_2O (Fig. 2C). The figure categorizes the values reported in literature based on whether H_2O and O_2 are included or omitted from the feeds of each system. The SCR values are further classified according to the four most commonly studied reductants: CO, hydrocarbons, NH_3 and H_2. Due to the inclusion of reductants in the SCR feed, direct decomposition of N_2O generally requires higher operating temperatures (300–600 °C) compared to the SCR of N_2O (150–500 °C), as shown in T_{50} values plotted in Fig. 2.[12,13]

Direct N_2O decomposition offers several industrial advantages, especially when N_2O emissions originate from high-temperature processes.[12] For example, N_2O emissions are often associated with the agricultural industry, ammonia combustion, adipic acid production, or fossil fuel combustion.[19] For these systems, direct decomposition may be favorable when emissions are released from high-temperature equipment, such as stoves/furnaces,[12,19] or following an ammonia combustion process.[20] Additionally, direct decomposition is often preferred in scenarios where introducing additional compounds into the system is undesirable. For instance, the addition of CO or NH_3 may elevate the risk of toxicity exposure hazards, create a stream of unreacted reactants that would require further processing, or result in the generation of additional greenhouse gas emissions.

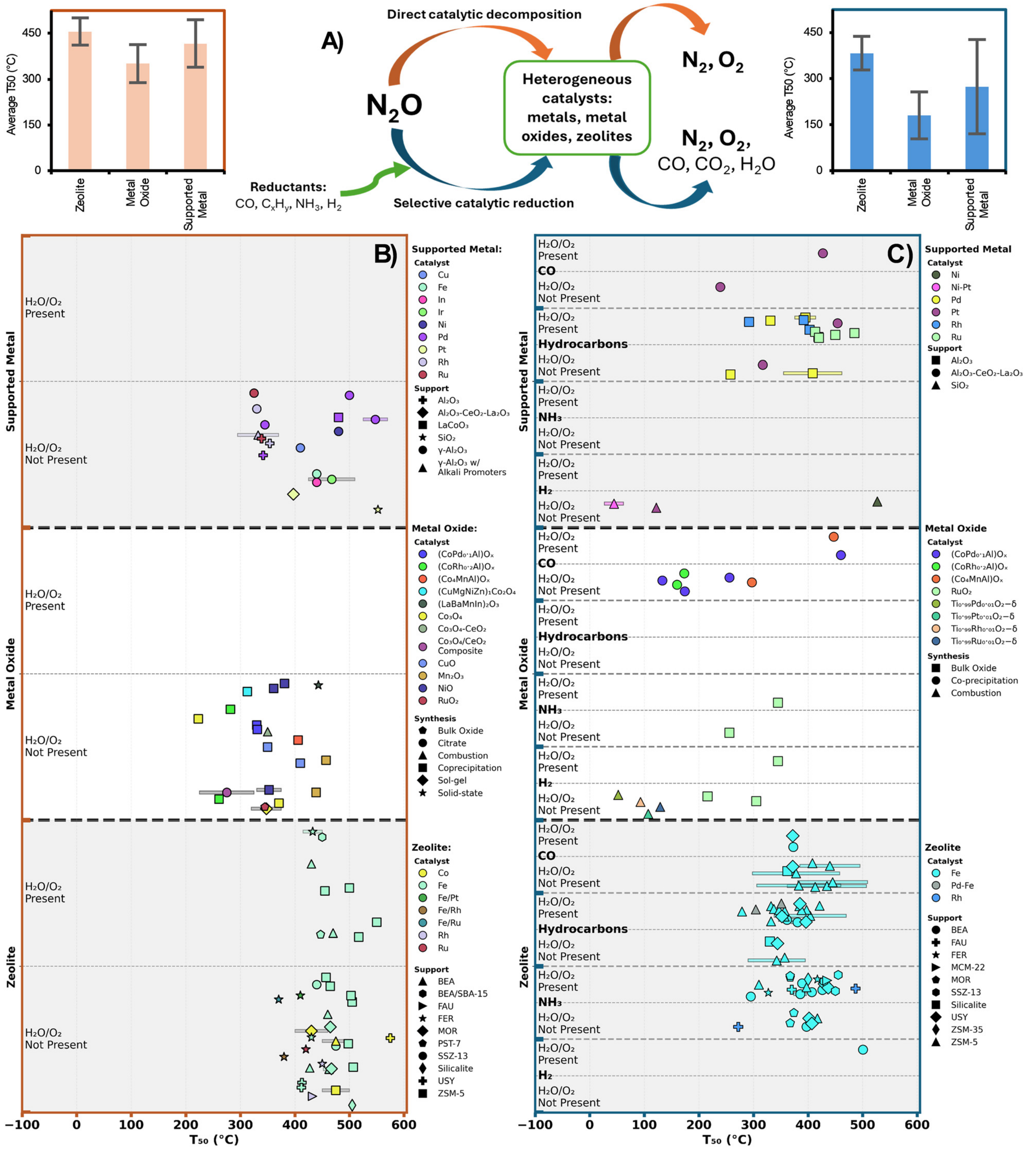

Fig. 2 (A) Reaction schemes for direct catalytic decomposition and SCR. T_{50} values for (B) direct decomposition (orange) and (C) SCR catalysts (blue). Note: three letter codes are given by the International Zeolite Association.

However, SCR of N_2O may be preferrable for applications that require lower operating temperatures or in industrial processes where suitable reductants are co-produced in tandem with N_2O. Moreover, some studies suggest that SCR reactions may be more applicable for treating exhaust from stationary or automotive sources.[8]

The choice of catalyst introduces additional considerations. Noble metal catalysts are known to show high activity, with Rh/CeO_2 being considered as one of the most active catalysts for this reaction.[21,22] However, these catalysts are limited by their high cost, abundance in nature, and global production constraints.[23] Cost-effective alternatives include transition metal oxides or zeolites, which have been shown to achieve low T_{50} values (as shown in Fig. 2). Many of the metals used in these catalysts are more abundant than noble metals, making metal oxides and zeolite catalysts attractive.[23] Zeolites offer further advantages, such as hydrothermal stability (in some applications) as well as acidity, which may offer beneficial catalytic properties.[24–26]

2 Direct nitrous oxide decomposition

Abatement *via* direct decomposition of N_2O proceeds without a reducing agent to produce N_2 and O_2 (eqn (1)).

$$2\ N_2O \rightarrow 2\ N_2 + O_2 \tag{1}$$

N_2O gas-phase catalytic mechanisms generally occur by having N_2O adsorb onto the catalyst active site (*) *via* the oxygen atom (eqn (2)). The N–O bond is then cleaved, releasing N_2 and leaving oxygen adsorbed on the surface.[27,28] The adsorbed oxygen removal process is slow in comparison.[29] Subsequently, the Eley–Rideal (E–R) or Langmuir–Hinshelwood (L–H) mechanism proceeds. For the E–R mechanism, an additional N_2O molecule interacts with the adsorbed atomic oxygen to produce O_2 and N_2 (eqn (3) and (4), Fig. 3). For the L–H mechanism, two adsorbed oxygen atoms recombine and then release O_2 (eqn (5), Fig. 3).

$$N_2O + * \rightarrow N_2 + O^* \tag{2}$$

$$N_2O + O^* \rightarrow N_2 + O_2^* \tag{3}$$

$$O_2^* \rightarrow O_2 + * \tag{4}$$

$$2\ O^* \rightarrow O_2 + 2^* \tag{5}$$

The Mars–van Krevelen mechanism is commonly suggested for many redox reactions, but it is not often observed in the direct decomposition of N_2O. By employing *in situ* XPS and DFT methods, Sun *et al.* demonstrated that the direct N_2O decomposition over single-atom Ru on CeO_2 nanorods proceeds *via* the Mars–van Krevelen mechanism.[30] Notably, oxygen desorption and oxygen vacancy formation are facilitated by the recombination of oxygen atoms that dissociate from N_2O with adjacent lattice oxygen. The Mars–van Krevelen mechanism is discussed more in section 3 and depicted in Fig. 7B, where an oxygen vacancy is created by a reductant to facilitate the N_2O reaction.

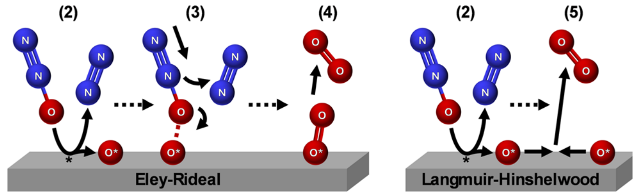

Fig. 3 Schematics of the Eley–Rideal and Langmuir–Hinshelwood mechanisms for N_2O decomposition. ("*" denotes surface site or adsorbed species). The numbers refer to the equations found in the text.

Regardless of the mechanism, the O_2 desorption step is crucial to the catalyst performance for N_2O decomposition due to the inhibitory effects of O_2. Multiple studies report decreased conversion and reaction rates with excess O_2 present across various catalysts.[31–33] O_2 often competes for binding sites and is slow to desorb from the catalyst. Therefore, catalyst discovery is necessary to aid in the desorption of oxygen from the surface of the catalyst to obtain increased conversion.

Several different catalyst designs have been utilized and modified in attempts to decompose N_2O and are considered by the following main categories: supported metal, metal oxide, and zeolite catalysts. These three types of catalysts will be discussed for N_2O decomposition, and a summary of the catalysts with corresponding activities is shown in Table 1 and Fig. 2B.

2.1 Supported metal catalysts

Many studies have suggested that Rh/CeO_2 is one of the more active catalysts for the direct decomposition of N_2O.[21] In one comprehensive study conducted by Li *et al.*, the researchers found that the synthesis of Rh/CeO_2 catalysts was important to increase activity.[21] The authors found that the calcination temperature of the supported Rh/CeO_2 catalysts led to an increase in activity (by a decrease in T_{50} value from ~355 °C for catalysts calcined at 500 °C to ~325 °C for catalysts calcined at 800 °C). They found further enhancement of catalytic activity by first calcining the support (CeO_2) at 800 °C where the T_{50} value was further reduced to ~310 °C.[21] Furthermore, Zhang *et al.* found that steam treating the catalyst allowed for a more water tolerant Rh/CeO_2 catalyst.[22] Though it is generally accepted that Rh is the most active metal for the abatement of N_2O, previous studies have looked at the activity of the different platinum group metals (*i.e.*, Rh, Pt, Pd, Ru, and Ir) and compared them to the activity of transition metals, which may provide cheaper alternatives. Pekridis *et al.* analyzed the impact of utilizing Pd, Rh, Ru, Cu, Fe, In, and Ni at 2 wt% supported on γ-Al_2O_3 (Fig. 4A).[32] It was found that the three noble metals (Pd, Ru, and Rh) exhibited the highest activity with the lowest T_{50} of ~325 °C. Of the transition metals, Cu exhibited the highest activity with a T_{50} of ~400 °C. Though the Cu-supported catalyst outperformed the other transition metal-supported catalysts, the noble metal catalysts still showed superior activity.[32] The authors attributed the difference in activity to the strength of oxygen adsorption on the surface. When testing noble metal catalysts in a reactant feed with excess O_2, all T_{50} values shifted towards higher temperatures; however, the increase in T_{50} for the noble metals was about 25 °C compared to the shift of 50 °C for the transition metals, which is likely a result of the higher electron density of the noble metals to efficiently facilitate oxygen desorption.[32]

Table 1 Summary of N_2O direct decomposition catalysts, grouped by catalyst type: supported metal catalysts (top), metal oxide catalysts (middle), and zeolite catalysts (bottom). T_{50} represents the temperature at which 50% conversion is reached, with flow conditions being defined by the gas hourly space velocity (GHSV), weight hourly space velocity (WHSV), or ratio of catalyst weight to volumetric gas flow rate (*W*/*F*). Note: GHSV, WHSV, and *W*/*F* were standardized based on feed conditions presented in the literature source for further comparison

Metal	Support	Catalyst synthesis	Reaction pretreatment	Feed composition	GHSV (h^{-1})	WHSV (h^{-1})	*W*/*F* (g s mL^{-1})	T_{50} (°C)	Ref.
Rh (1 wt%)	CeO_2	Dry impregnation followed by steam treatment		0.3% N_2O/He			0.018	~273	22
Rh (1 wt%)	CeO_2	Dry impregnation		200 ppm N_2O/5% CO_2/N_2	30 000			~310	21
Ru (2 wt%)	γ-Al_2O_3	Dry impregnation	He: 600 °C/1 h	0.12% N_2O/He	35 000			~325	32
Rh (2 wt%)	γ-Al_2O_3	Dry impregnation	He: 600 °C/1 h	0.12% N_2O/He	35 000			~330	32
Pd (2 wt%)	γ-Al_2O_3	Dry impregnation	He: 600 °C/1 h	0.12% N_2O/He	35 000			~345	32
Cu (2 wt%)	γ-Al_2O_3	Dry impregnation	He: 600 °C/1 h	0.12% N_2O/He	35 000			~410	32
Fe (2 wt%)	γ-Al_2O_3	Dry impregnation	He: 600 °C/1 h	0.12% N_2O/He	35 000			~440	32
In (2 wt%)	γ-Al_2O_3	Dry impregnation	He: 600 °C/1 h	0.12% N_2O/He	35 000			~440	32
Ni (2 wt%)	γ-Al_2O_3	Dry impregnation	He: 600 °C/1 h	0.12% N_2O/He	35 000			~480	32
Pt (0.25–1 wt%)	γ-Al_2O_3	Dry impregnation	He: 600 °C/1 h	0.1% N_2O/He	40 000				33
Ir (0.25–1 wt%)	γ-Al_2O_3	Dry impregnation	He: 600 °C/1 h	0.1% N_2O/He	40 000			425–510	33
Pd (0.25–1 wt%)	γ-Al_2O_3	Dry impregnation	He: 600 °C/1 h	0.1% N_2O/He	40 000			525–570	33
Rh (0.5 wt%)	CeO_2	Dry impregnation		1000 ppm N_2O/He	10 000				27
Rh (0.5 wt%)	γ-Al_2O_3	Dry impregnation		1000 ppm N_2O/He	10 000				27
Pd (1 wt%)	$LaCoO_3$	Impregnation		1000 ppm N_2O/1000 ppm NO/He			0.168	~480	34
Pd (1 wt%)	γ-Al_2O_3	Impregnation		1000 ppm N_2O/1000 ppm NO/He			0.168	~500	34
Rh (1 wt%)	γ-Al_2O_3	Dry impregnation		200 ppm N_2O/5% O_2/N_2	30 000				35
Rh (1 wt%)	CeO_2	Dry impregnation		200 ppm N_2O/5% O_2/N_2	30 000				35
Rh (0.1 wt%)	γ-Al_2O_3 with alkali promoters	Impregnation		1% N_2O/N_2	4000			295–370	36
Rh (2 wt%)	ZrO_2 with Pd as a promoter	Impregnation		1000 ppm N_2O/He			0.02	307	37
Pt (0.5 wt%)	Al_2O_3–CeO_2–La_2O_3	Co-precipitation, impregnation	H_2/He, 400 °C, 1 hHe, 400 °C, 1 h	0.1% N_2O, He balance	10 000			397	38
Ru (2 wt%)	Al_2O_3	Dry impregnation		500 ppm N_2O, He balance			0.12	339	39
Rh (2 wt%)	Al_2O_3	Dry impregnation		500 ppm N_2O, He balance			0.12	354	39
Pd (2 wt%)	Al_2O_3	Dry impregnation	He, 100 cm^3 min^{-1}, 600 °C, 1 h	0.12% N_2O, He balance	35 000			342	40
Pt (2 wt%)	SiO_2	Incipient wetness impregnation	H_2, 400 °C, 1 h	1250 ppm N_2O, He balance	25 000			552	41

Oxide	Dopant/promoter	Catalyst synthesis	Reaction pretreatment	Feed composition	GHSV (h^{-1})	WHSV (h^{-1})	*W*/*F* (g s mL^{-1})	T_{50} (°C)	Ref.
MnO			He: 120 °C/45 min then 500 °C/90 min	0.066 atm N_2O/N_2	2000				42
Mn_3O_4			He: 120 °C/45 min then 500 °C/90 min	0.066 atm N_2O/N_2	2000				42
Mn_2O_3			He: 120 °C/45 min then 500 °C/90 min	0.066 atm N_2O/N_2	2000				42
MnO_2			He: 120 °C/45 min then 500 °C/90 min	0.066 atm N_2O/N_2	2000				42

Table 1 *(continued)*

Oxide	Dopant/promoter	Catalyst synthesis	Reaction pretreatment	Feed composition	GHSV (h^{-1})	WHSV (h^{-1})	W/F ($g\ s\ mL^{-1}$)	T_{50} (°C)	Ref.
Co_3O_4				5% N_2O/Ar	80 000			<700	31
CuO	CeO_2 (nanorods)	CeO_2: hydrothermal CuO/CeO_2: precipitation	Ar: 400 °C/1 h	2500 ppm N_2O/Ar					43
Co_3O_4/CeO_2 composite oxide	Li, Na, K, Rb, Cs, Mg, Ca, Sr, Ba	Citrate method	20% O_2/Ar: 400 °C/30 min	1000 ppm N_2O/Ar			0.2	225–325	44
Co_3O_4	Cs	Coprecipitation		1000 ppm N_2O/N_2	30 000			223	45
CuO	Cs	Coprecipitation		1000 ppm N_2O/N_2	30 000			350	45
NiO		Coprecipitation		1000 ppm N_2O/N_2	30 000			361	45
Co_3O_4		Coprecipitation		1000 ppm N_2O/N_2	30 000			371	45
NiO	Cs	Coprecipitation		1000 ppm N_2O/N_2	30 000			381	45
CuO		Coprecipitation		1000 ppm N_2O/N_2	30 000			410	45
Mn_2O_3		Coprecipitation		1000 ppm N_2O/N_2	30 000			439	45
Mn_2O_3	Cs	Coprecipitation		1000 ppm N_2O/N_2	30 000			457	45
Co_3O_4–CeO_2	Rb	Combustion method employing urea	N_2: 500 °C/1 h	500 ppm N_2O/N_2			0.15	~350	46
Co_3O_4	Sm	Sol–gel method with citric acid and urea		1000 ppm N_2O/N_2			0.06	~320–375	47
NiO	Pr	Coprecipitation		800 ppm N_2O/N_2			0.06	~330–375	48
Co_3O_4	Ce–Pr	Coprecipitation		800 ppm N_2O/N_2	60 000			317	49
Co_3O_4	K–Dy	Sol–gel	Ar: 400 °C/30 min	2000 ppmv N_2O/Ar	20 000			~225–240	50
Co_3O_4	K–Dy	Co-precipitation and impregnation	Ar: 500 °C/30 min	2000 ppmv N_2O/Ar	20 000			~225	51
Co_3O_4	Bi	Sol–gel	Ar: 400 °C/30 min	2000 ppmv/Ar			0.24	~250	52
Co_3O_4	F	Co-precipitation		1000 ppm/Ar	10 000			310	53
Co_3O_4	N	g-C_3N_4-modified thermal decomposition		1000 ppmv N_2O/Ar	10 000			~260	54
Co_3O_4	NiO–Y_2O_3	Co-precipitation		1000 ppmv N_2O/Ar	10 000			~275	55
RuO_2		Bulk oxide	He, 400 °C, 1 h	N_2O (1.5 mbar), He balance		5.4		345	56
$(CuMgNiZn)_1Co_2O_4$		Coprecipitation		1000 ppm N_2O/N_2	60 000			313	57
$La_{0.7}Ba_{0.3}Mn_{0.8}In_{0.2}O_3$		Solid-state		10% N_2O/He			3.0	~443	58
$(CoRh_{0.2}Al)O_x$ mixed oxide		Co-precipitation of hydrotalcite-type precursors	N_2, 500 °C, >3 h	12 500 ppm N_2O, N_2 balance	30 000			261	59
$(CoPd_{0.1}Al)O_x$ mixed oxide		Co-precipitation of hydrotalcite-type precursors	N_2, 500 °C, >3 h	12 500 ppm N_2O, N_2 balance	30 000			330	59
$(Co_4MnAl)O_x$ mixed oxide		Co-precipitation of hydrotalcite-type precursors	He, 450 °C, 1 h	0.1 mol% N_2O, He balance			0.06	406	60
$(CoRh_{0.2}Al)O_x$ mixed oxide		Co-precipitation of hydrotalcite-type precursors		12 500 ppm N_2O, N_2 balance	30 000			274–290	61
$(CoPd_{0.1}Al)O_x$ mixed oxide		Co-precipitation of hydrotalcite-type precursors		12 500 ppm N_2O, N_2 balance	30 000			328–334	61

Metal	Zeolite base	Catalyst synthesis	Reaction pretreatment	Feed composition	GHSV (h^{-1})	WHSV (h^{-1})	W/F ($g\ s\ mL^{-1}$)	T_{50} (°C)	Ref.
Cu	SSZ-13	Ion exchange	Air: 500 °C/30 min	500 ppm N_2O/N_2			0.0031		28

Table 1 *(continued)*

Metal	Zeolite base	Catalyst synthesis	Reaction pretreatment	Feed composition	GHSV (h^{-1})	WHSV (h^{-1})	W/F (g s mL^{-1})	T_{50} (°C)	Ref.
Co	SSZ-13	Ion exchange	Air: 500 °C/30 min	500 ppm N_2O/N_2			0.0031		28
Fe	SSZ-13	Ion exchange	Air: 500 °C/30 min	500 ppm N_2O/N_2			0.0081		28
Co	MOR	Wet ion exchange	He: 600 °C/1 h	5000 ppm N_2O/He	30 000			~400–460	62
Co	ZSM-5	Wet ion exchange	He: 600 °C/1 h	5000 ppm N_2O/He	30 000			~450–500	62
Co	BEA	Wet ion exchange	He: 600 °C/1 h	5000 ppm N_2O/He	30 000			~450–500	62
Co	USY	Wet ion exchange	He: 600 °C/1 h	5000 ppm N_2O/He	30 000			~575	62
Fe/Ru	FER	Ion exchange		1000 ppm N_2O/He	90 000			~360	63
Fe/Rh	FER	Ion exchange		1000 ppm N_2O/He	90 000			~380	63
Fe/Pt	FER	Ion exchange		1000 ppm N_2O/He	90 000			~410	63
Ru	FER	Ion exchange		1000 ppm N_2O/He	90 000			~420	63
Fe	FER	Ion exchange		1000 ppm N_2O/He	90 000			~430	63
Rh	FER	Ion exchange		1000 ppm N_2O/He	90 000			>450	63
Fe	FER	Ion exchange	Air: 550 °C/2 h	0.2% N_2O/3.0% O_2/He	35 000			~417–437	64
Fe	BEA	Ion exchange	Air: 550 °C/2 h	0.2% N_2O/3.0% O_2/He	35 000			~467–477	64
Fe	ZSM-5	Ion exchange	Air: 550 °C/2 h	0.2% N_2O/3.0% O_2/He	35 000			~497–507	64
Fe	SSZ-13	Ion exchange	14% O_2/N_2: 500 °C/1 h	540 ppm N_2O/N_2	200 000			~440	24
Fe	BEA	Ion exchange	14% O_2/N_2: 500 °C/1 h	540 ppm N_2O/N_2	200 000			~460	24
Fe	PST-7	Hydrothermal	Air: 550 °C/2 h	1000 ppm N_2O/4% O_2/He	42 000			447	65
Fe	ZSM-5	Hydrothermal	Air: 550 °C/2 h	1000 ppm N_2O/4% O_2/He	42 000			517	65
Fe	SBA-15	Ion exchange	He: 550 °C/1 h	5000 ppm N_2O/45 000 ppm O_2/He			0.12		26
Fe	BEA	Ion exchange	He: 550 °C/1 h	5000 ppm N_2O/45 000 ppm O_2/He			0.12	~430	26
Fe	BEA/SBA-15	Ion exchange	He: 550 °C/1 h	5000 ppm N_2O/45 000 ppm O_2/He			0.12	~450 °C	26
Fe	ZSM-5	Wet ion exchange + alkaline treatment of zeolite	Ar: 500 °C/30 min	5000 ppm N_2O/5% O_2/Ar	30 000			~455	66
Fe	ZSM-5	Wet ion exchange	Ar: 500 °C/30 min	5000 ppm N_2O/5% O_2/Ar	30 000			~550	66
Fe	BEA	Ion exchange	3% H_2/Ar, 13 cm^3 min^{-1}, ramp from 80–700 °C at 10 °C min^{-1}	0.2% N_2O, He balance	35 000			452–473	67
Fe	Silicalite	Hydrothermal, ion exchange, steam activation	N_2O/He, 450 °C, 1 h	N_2O (1.5 mbar), He balance		11.3		505	68
Fe	ZSM-5	Hydrothermal, ion exchange, steam activation	N_2O/He, 450 °C, 1 h	N_2O (1.5 mbar), He balance		11.3		505	68
Fe	ZSM-5	Sublimation	N_2O/He, 450 °C, 1 h	N_2O (1.5 mbar), He balance		10.8		465	69
Fe	ZSM-5	Isomorphous substitution, steam activation	N_2O/He, 450 °C, 1 h	N_2O (1.5 mbar), He balance		10.8		498	69
Fe	ZSM-5	Hydrothermal, ion exchange, steam activation	He, 450 °C, 2 h	N_2O (1.5 mbar), He balance	90 000			507	70
Fe	ZSM-5	Isomorphous substitution, ion exchange, steam activation	He, 450 °C, 2 h	N_2O (1.5 mbar), He balance	90 000			503	71
Fe	USY	Ion exchange	He, 600 °C, 1 h	5000 ppm N_2O, He balance	30 000			413	72
Fe	USY	Ion exchange	He, 600 °C, 1 h	5000 ppm N_2O, He balance	30 000			412	73
Fe	BEA	Ion exchange	He, 600 °C, 1 h	5000 ppm N_2O, He balance	30 000			427	73
Fe	MOR	Ion exchange	He, 600 °C, 1 h	5000 ppm N_2O, He balance	30 000			465	73
Fe	ZSM-5	Ion exchange	He, 600 °C, 1 h	5000 ppm N_2O, He balance	30 000			457	73
Fe	MOR	Ion exchange	He, 600 °C, 1 h	5000 ppm N_2O, He balance	30 000			467	74
Rh	FAU	Impregnation	Air, 500 °C	0.2% N_2O, He balance	30 000			432	75

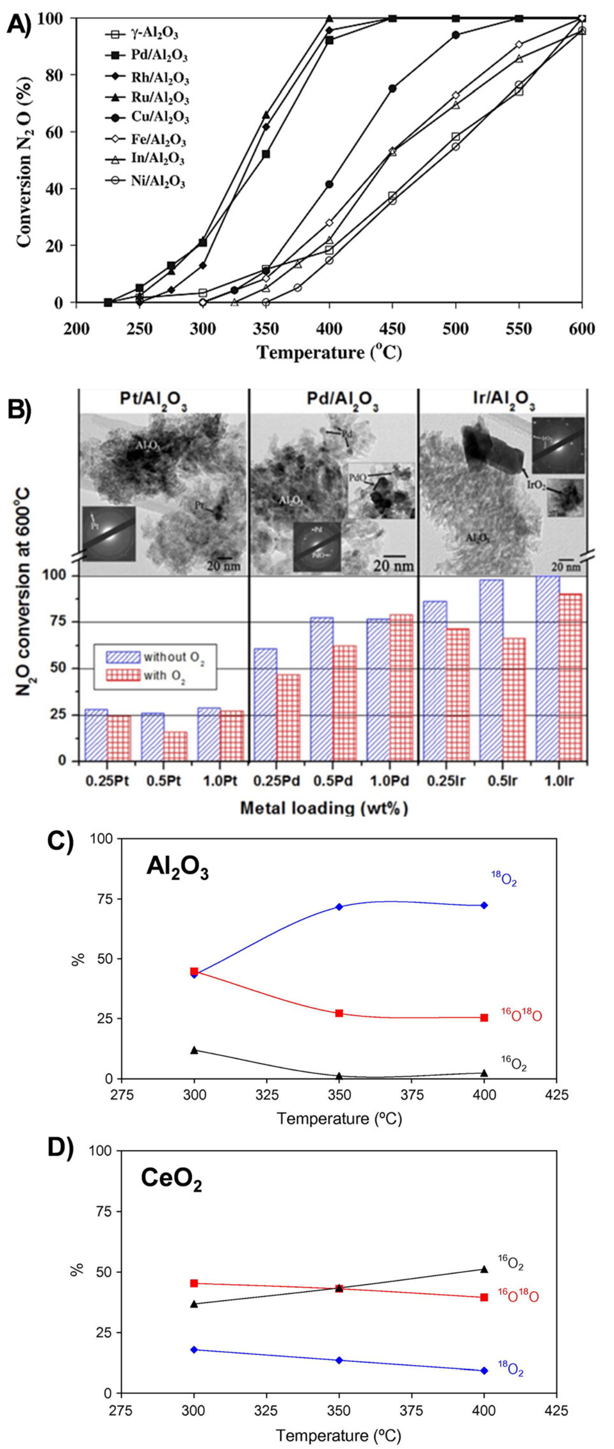

Fig. 4 (A) Comparison of catalytic activity for various Al_2O_3-supported metal catalysts (2 wt% metal tested at a GHSV = 35 000 h^{-1} with P_{N_2O} = 0.12% and a balance in He). Reprinted from ref. 32 with permission from Springer Nature. (B) N_2O conversion at 600 °C with and without O_2 for Pt, Pd, and Ir on alumina catalysts with insight to surface morphology. Reprinted from ref. 33 with permission from Elsevier. Oxygen content produced from isotopic $^{15}N_2{}^{18}O$ pulse experiment on 0.5 wt% Rh on (C) Al_2O_3 and (D) CeO_2 to show the evolution of oxygen species, highlighting the oxygen donating role of the CeO_2 support. C and D Reprinted from ref. 27 with permission from Elsevier.

Pachatouridou *et al.* investigated the impact of the weight loading of noble metals on the decomposition of N_2O. The effect of Pt, Pd, and Ir supported on γ-Al_2O_3 at various weight loadings showed that an increased metal loading led to increased N_2O conversion at lower temperatures, thus resulting in lower T_{50} numbers.[33] The Ir metal catalyst was found to have the highest activity in the absence of O_2. The addition of oxygen raised the T_{50} by ~100 °C, for the most active catalyst with 1 wt% Ir. The difference in activity was attributed to the ability of each metal to adsorb oxygen. In catalytic tests in both the presence and absence of O_2, Pt/Al_2O_3 was less active, while Ir- and Pd-based catalysts were less affected. The authors attributed the overall poor Pt performance to site blocking or competitive adsorption of O_2 to the active, metallic Pt surface, and the better Ir and Pd performances to oxide phases that are less susceptible to oxygen poisoning. When comparing the crystallite size from XRD and TEM, larger crystallites of IrO_2 (26.2 nm) were observed, as shown in Fig. 4B, which the authors suggested benefit the activity by easing oxygen desorption from defect-free surfaces, reducing oxygen-induced site blocking. Regardless of whether the high performance is from the active metal itself or properties derived from the support, oxygen desorption is essential to increase conversion due to competitive binding to active sites on the metal surface.

Parres-Esclapez *et al.* analyzed the activity of the Rh/CeO_2 catalyst on N_2O decomposition and found that CeO_2 had a higher rate of N_2O decomposition than Al_2O_3 catalysts.[27] The authors related the difference in rate to different physicochemical properties of the catalysts. They noted that the apparent activation energy for Rh/CeO_2 was ~25 kJ mol^{-1} less than that of the Rh/Al_2O_3, possibly indicating different mechanisms for decomposition on CeO_2 *versus* Al_2O_3. To elucidate the potential mechanisms over the catalysts, pulse decomposition experiments were conducted with $^{15}N_2{}^{18}O$. The study showed that the γ-Al_2O_3-supported catalyst produced $^{18}O_2$ as the primary product, which indicated that the majority of the oxygen produced was a result of oxygen atoms coming from N_2O *via* the Eley–Rideal mechanism. However, when conducting the same experiment with the Rh/CeO_2 catalysts at 350 °C, ~50% $^{18}O^{16}O$ evolved from the system. This indicated a more substantial participation of the support oxygen in the overall reaction mechanism. Therefore, the group noted the important role that the CeO_2 support plays in exchanging oxygen atoms from the surface of the support to produce molecular oxygen, which was not as prominent for the γ-Al_2O_3-supported catalysts to as great of an extent, as shown in Fig. 4C.[27]

Zhu *et al.* performed an *in situ* diffuse reflectance infrared Fourier transform spectroscopy (DRIFTS) experiment with Rh/CeO_2 catalysts.[35] The DRIFTS measurements showed N_2O adsorption peaks both on the Rh sites and CeO_2 support, indicating that both the metal and support play a role in the reaction mechanism, as also observed by Parres-Esclapez *et al.*[27,35] Prior to N_2O-DRIFTS, the samples were reduced, facilitating the formation of Ce^{3+} sites, or oxygen vacancies. The N_2O-DRIFTS data showed that the support can be oxidized under N_2O, from Ce^{3+} to Ce^{4+}, providing insight into the redox abilities and role of supports in the N_2O decomposition mechanism.[35] However, the authors noted that Ce^{4+} was not reduced to Ce^{3+} in their experiments at room temperature, indicating O_2 desorption as a rate-limiting step.

The role of supports on N_2O decomposition has been further studied by Yoshida *et al.*, where Pt and Pd catalysts on SiO_2–Al_2O_3, SiO_2, Al_2O_3, ZrO_2, MgO (listed from most acidic to least acidic) supports were investigated.[76] The study aimed to relate how the acidity of the support impacts the oxidation and reduction properties of the catalysts, which is of concern due to the oxidative nature of the reaction. The researchers found that more acidic supports can suppress oxidation of the metal at lower temperatures, which can promote the desorption of O_2 and increase conversion. This suggests that the support can aid in resisting oxygen site blocking and further enhance the reaction conversion.

Similarly, Dacquin *et al.* studied a Pd-supported catalyst on γ-Al_2O_3 and $LaCoO_3$.[34] When comparing the N_2O conversion during a temperature programmed experiment using a mixed stream of dry 1000 ppm NO and 1000 ppm N_2O gases, it was found that the conversion increased from 15% on Pd/Al_2O_3 to 32% on Pd/$LaCoO_3$ at 460 °C, and the apparent activation energy decreased from ~93 to ~55 kJ mol^{-1}. The authors concluded that the increase in conversion and lower barrier arises from an interaction between the Pd and the reducible $LaCoO_3$ support that can create anionic oxygen vacancies and supplies labile oxygen species, as seen with the increased intrinsic activity ceria.[27,34]

The inclusion of promoters can have an equally impactful role as the support on N_2O decomposition. Haber *et al.* found that alkali-metal promoters further enhanced the N_2O decomposition reaction by increasing metallic dispersion (prior to reaction).[36] The study examined a series of Rh/γ-Al_2O_3 catalysts with various alkali promoters. The Cs promoted catalyst gave the overall lowest T_{50} number (T_{50} performance based on promoters ranked from lowest to highest: Cs, K, Li, Na). The Li and Na-promoted catalysts experienced a clear optimum weight loading at 0.078 mol% of alkali metal oxide, whereas the Cs and K-promoted catalysts did not exhibit such a sharp optimum. The improved activity for the catalysts with larger alkali metals was attributed to an increased Rh dispersion, resulting from an electron-donating effect from the promoters. X-ray photoelectron spectroscopy (XPS) confirmed that the alkali metals increased the electron-density/charge effect on support oxygen, which may hinder Rh diffusion and suppress particle growth. In addition, Pd has been found to have a promotional effect towards Rh/ZrO_2 catalysts.[37] Zhang *et al.* found that not only did Pd enhance the catalytic activity and decrease the overall activation energy but also influenced the ability to reduce Rh species to their active state and promote the formation of oxygen vacancies. Though also inhibited by O_2, CO_2, and H_2O, Pd promoted Rh catalysts still showed lower T_{50} values than the baseline Rh/ZrO_2 catalyst.[37]

Novel catalysts will continue to be researched to drive innovation and progress towards zero-emission processes. Single-atom catalysts (SACs) dispersed on a support have also been explored due to their high atom efficiency and unique electronic properties.[77] Liu *et al.* synthesized a Pt SAC on a $MgAl_{1.2}Fe_{0.8}O_4$ spinel. Subsequent testing of the catalysts for N_2O decomposition revealed that the Pt SAC (calcined at 800 °C) had the lowest T_{50}, while the incipient wetness impregnation (IWI) catalyst (calcined at 300 °C) had the highest T_{50}.[78] Sun *et al.* developed a single-atom Ru on CeO_2 nanorods catalyst with an ultralow Ru loading of 0.48 wt% for the direct N_2O decomposition.[30] Using a combined experimental and computational approach, they found that the Ru/CeO_2 SAC outperformed the Ru/CeO_2 nanoparticles due to enhanced O_2 desorption and showed high O_2 resistance. On the contrary, by controlled synthesis and comparing Rh single atoms, nanoclusters (1.1 nm), and nanoparticles (2.1 nm) supported on defect-rich CeO_2, Bao *et al.* reported that Rh nanoclusters exhibited a superior activity for direct N_2O decomposition compared to SAC and nanoparticles.[79] The recombination and desorption of oxygen were facilitated by the adjacent Rh atoms in the Rh cluster and positively charged Rh species. In addition to SACs, metal–organic frameworks (MOFs), which are highly porous three-dimensional crystalline materials composed of metal ions or clusters coordinated to organic ligands, are emerging as versatile and effective catalysts owing to their high surface area, tunable porosity, and customizable chemical functionality.[80] Palladium-loaded, metal–organic framework (MOF)-derived catalysts were developed with controlled thermal treatment to improve Pd dispersion for synergistic N_2O decomposition and CO oxidation.[81] They found that the (2%Pd/MIL)-*T* catalyst is highly active and achieved full N_2O decomposition at 550 °C under a space velocity of 240 000 ml h^{-1} g_{cat}^{-1}, which outperformed the commercial Pd/Cr_2O_3 and previous MOF-based catalysts. Tang *et al.* utilized ZIF-67 frameworks as precursors for preparing Co/CoO_x@carbon catalysts for direct N_2O decomposition and achieved a low T_{50} value of 305 °C.[82] It was noted that the ZIF67-derived amorphous graphitic carbon frameworks are instrumental in transferring/storing active oxygen and regenerating cobalt active centers. A hollow porous NiO@CeO_2 octahedron catalyst derived-from cerium-based metal–organic frameworks was prepared by Zhao *et al.* and showed a high activity for the N_2O decomposition.[83] By employing various characterization techniques, this remarkable catalytic performance was attributed to the hollow porous structures, uniform Ni dispersion, and large amount of oxygen vacancies in the MOF-derived Ni/CeO_2 catalyst.

2.2 Metal oxides

The scarcity and price of precious metals continuously drive research to find alternative catalysts that provide increased conversion at a lower cost. Therefore, improving the desorption of oxygen and regeneration of active sites for transition metal oxides and mixed oxide catalysts, such as Co, Mn, Cu, and Ni oxides, is essential to identify precious metal alternative catalysts for N_2O decomposition.[31,42,43,45,48] For metal oxides, the metal sites tend to exhibit various oxidation states, which can influence the complexity of the catalyst and reaction conversions.

Yamashita and Vannice analyzed the different oxidation states of Mn oxide catalysts to determine the most active oxidation state of Mn.[42] The study analyzed the performance of MnO, Mn_3O_4, Mn_2O_3, and MnO_2 and found that Mn_2O_3 had the largest sustained N_2O decomposition rate of 1400×10^{-4} μmol s^{-1} $g_{cat}{}^{-1}$, compared to MnO, which had a rate of 6.3×10^{-4} μmol s^{-1} $g_{cat}{}^{-1}$. When analyzing the decomposition products, the Mn_2O_3 catalyst produced stoichiometric decomposition products compared to the MnO catalyst, which only produced N_2 as a product. The authors indicate that other Mn oxides were being oxidized to Mn_3O_4, thus hindering the overall catalytic performance,[42] where it is concluded that the Mn^{3+} oxidation state is the active site for this reaction.

There have been additional studies conducted to elucidate the mechanism for N_2O decomposition. Jing *et al.* conducted *operando* XAS studies to better understand the decomposition mechanism on a RhO_x/ZrO_2 catalyst, which displayed high activity in an N_2O environment as well as with other inhibitors, such as O_2 and H_2O. In their study, the catalysts were first treated with a heating step.[84] In conducting *in situ* XANES, the researchers elucidated that the heating step allowed for an initial reduction of Rh, forming defect sites on the catalyst. Following this study, the group introduced 1% N_2O to their sample and analyzed the effluent with a GC while analyzing the catalyst using XANES. When conducting their study, the group found that the XANES spectra shifted to higher energy. Simultaneously, they saw N_2 and O_2 in the effluent from their GC data. The authors suggested that this displayed how the N_2O acted as an oxidizing agent to the Rh. Relating this to the *in situ* XANES that was conducted, the authors suggested that the defect sites formed during the high temperature treatment facilitated the decomposition of N_2O, further displaying how this reaction proceeded *via* a redox mechanism. Another *operando* study conducted by Jing *et al.* elucidated the impact of adding Ag as a promoter to a RhO_x/Al_2O_3 catalyst.[85] From their study using *operando* diffuse reflectance UV-vis, they found that the silver promotes the reduction of the Rh species, which is necessary to form defect sites for the reaction to occur as they previously found.[84,85]

In addition to identifying catalyst active sites, the influence of common inhibitors is important in understanding the functionality of the catalyst. Wilczkowska *et al.* analyzed the possible activation and deactivation mechanisms due to the presence of O_2 or H_2O in the feed stream for a Co oxide spinel catalyst.[31] They found that O_2 inhibited the reaction at lower temperatures (<800 °C), but increased activity at higher temperatures compared to experiments when O_2 was not present in the feed. The authors noted that the initial reduced activity at lower temperatures in the presence of O_2 can be attributed to competitive adsorption of O_2 on the active sites, creating a saturated Co species. XRD analysis revealed that the addition of O_2 in the feed stabilized the active Co_3O_4 state at higher temperatures, whereas in an anoxic environment, the catalyst was reduced to CoO. When H_2O was present in the feed, the activity had decreased with XRD revealing the catalyst to be reduced, while H_2O blocked active sites due to competitive adsorption. This result was further confirmed from XPS with an increase in the ratio of O_{ads}/O_{latt} (where O_{ads} and O_{latt} are the oxygen associated with hydroxyl groups and the lattice, respectively) when H_2O was present in the feed.[31] This was attributed to the competitive adsorption on the surface of the cobalt oxide catalyst.

Many studies have aimed to identify dopants and promoters that will both enhance the reaction as well as regenerate the active centers. Zabilskiy *et al.* sought to understand the role of incorporating CuO supported on CeO_2 nanorods.[43] Through XPS, the addition of CeO_2 to the catalyst was found to facilitate the increase in anion defect sites (oxygen vacancies). High-angle annular dark-field scanning transmission electron microscopy showed that the surface of the catalysts was enriched with Ce^{3+} while the bulk was enriched with Ce^{4+}. The authors attributed this to the ability of Ce to generate labile oxygens to regenerate the active Cu^+ sites, which is portrayed in Fig. 5A.[43] In addition, an increased activity for CuO on CeO_2 was correlated to Ce^{3+} ions, determined by *operando* ultraviolet-visible spectroscopy (UV-vis).[43] It was concluded that a $[Cu–O–Cu]^{2+}$ species is formed on the surface with labile oxygens from the CeO_2 support donating species to help promote the formation of the active copper complexes.[43]

Some studies have also been performed on the role of alkali and alkali earth promoters on metal oxide catalysts. Xue *et al.* studied the incorporation of alkali and alkali earth metals into a cobalt–cerium composite oxide catalyst.[44] The study determined that the alkali metal-promoted oxide had lower T_{50} numbers, with Cs showing the best T_{50} of ∼225 °C (compared to the unpromoted oxide, T_{50} of ∼350 °C), as shown in Fig. 5B. The authors attributed this impact to an electronic effect on Co^{2+}.[44] This was further evidenced with O_2-temperature programmed desorption (TPD) and H_2-TPR. The authors found that larger-element alkali-promoted catalysts facilitated O_2 desorption at lower temperatures due to having a lower overall desorption intensity, while there was an increase in reducibility to regenerate the Co^{2+} site as evidenced with H_2-TPR. This indicated that the alkali metals donate electrons to facilitate oxygen desorption and increase N_2O conversion to regenerate the active site.[44]

Zhao *et al.* sought to understand the impact of utilizing Cs as a promoter on common oxides, such as Co_3O_4, CuO, NiO, and Mn_2O_3.[45] The study found that the addition of Cs, as the most basic alkali metal, had a positive impact on the

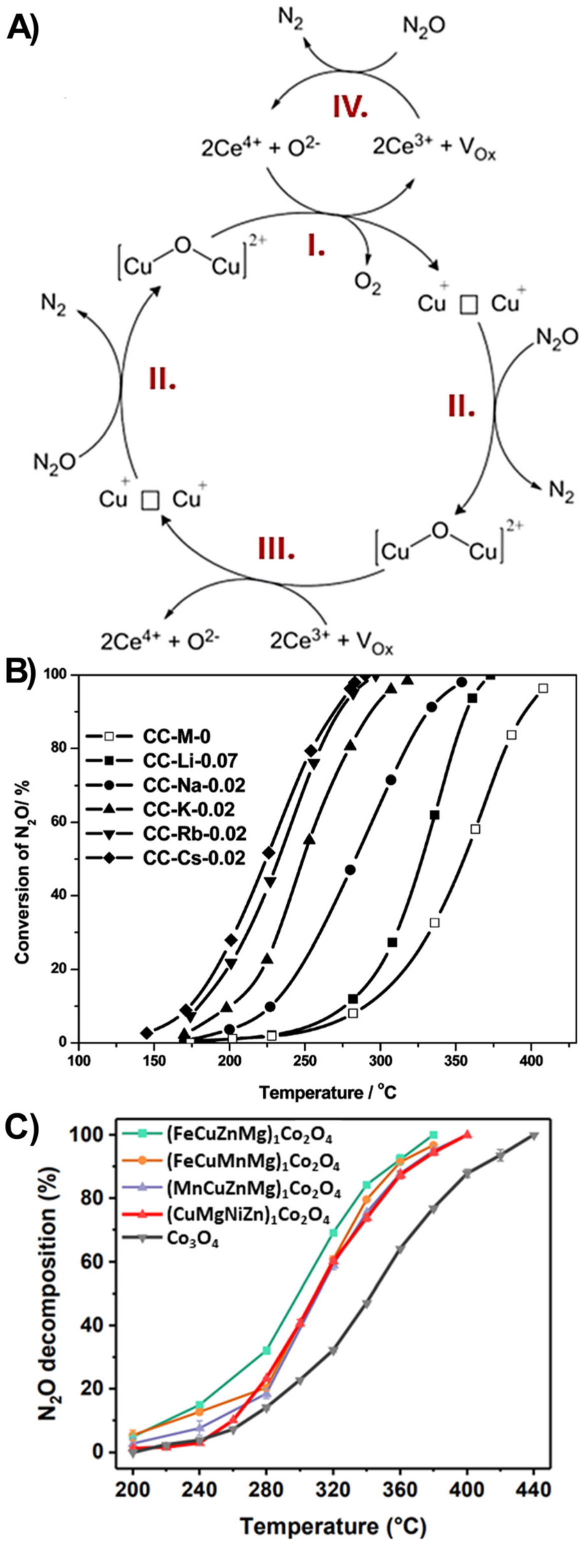

Fig. 5 (A) A proposed N_2O decomposition mechanism for a CuO/CeO_2 oxide catalysts. Adapted from ref. 43 with permission from Elsevier. (B) Light-off curve plots of alkali metal promoted cobalt–cerium composite oxides. Reprinted from ref. 44 with permission from the American Chemical Society. (C) Light-off curve plots for spinel Co_3O_4-based HEOs. Adapted from ref. 57 with permission from the American Chemical Society.

Co_3O_4 and CuO catalysts and an inhibiting impact for NiO and Mn_2O_3 catalysts (an increased T_{50} number). For Co_3O_4, the T_{50} number decreased by ~150 °C from the unpromoted catalyst and outperformed the worst-performing catalyst (Cs/Mn_2O_3) by ~235 °C. This change in activity was accompanied by a decrease in activation energy for the Co and Cu catalysts and an increase in activation energy for the Ni and Mn (inhibited) catalysts. For the Cs/Co_3O_4 catalyst, XPS showed an increase in the Co^{3+} fraction (considered the active center of the catalyst) with increasing Cs concentration. In addition, the authors found that the O 1s peak of the Co was shifted to lower binding energies (529.8 eV to 529.4 eV) when promoted with Cs, indicating a potential electronic effect through the donation of electrons to the active center. Additionally, H_2-TPR showed that the first metal reduction peak of Cs promoted Co-based catalysts was shifted to lower temperatures. However, the second reduction peak for Co-based catalysts and all of the reduction peaks for the Cu-based catalysts were shifted to higher temperatures, indicating that Cs donated electrons to stabilize the active centers of these catalysts. When compared to Ni and Mn catalysts, which experienced poorer performance when doped with Cs, the TPR reduction peaks shifted slightly, indicating a lesser ability to be reduced, possibly explaining the decreased performance.[45]

Abu-Zied *et al.* chose to incorporate Rb into a Co_3O_4–CeO_2 mixed oxide catalyst and analyzed the impact of changing the dopant concentration from 0.0125–0.2 ratio of Rb to Co.[46] Similarly to Zhao *et al.*, they found that the role of Rb was to enhance the ability of Co^{2+} to donate electrons to the N_2O to facilitate decomposition.[45,46] This was confirmed through XPS results as well as a decrease in the T_{50} number for the Rb fraction of 0.025 (T_{50} was ~350 °C compared to the unpromoted cobalt oxide, which was about 450 °C).[46]

Despite numerous studies analyzing the impact of promoters, there have been few studies that sought to examine more "exotic" promoters, such as lanthanides. Lanthanides are known to have increased redox properties due to having an unfilled 4f orbital.[47] Liu *et al.* analyzed the impact of doping Co_3O_4 catalysts with samarium (Sm). Through *in situ* XPS experiment that exposed the catalyst to 5000 ppm of N_2O at various temperatures, the authors saw that there was no difference (or shift) in the Co 2p XPS spectrum under reaction conditions, indicating a stable Co active site. However, the Sm 3d spectra shifted to higher binding energies throughout the exposure to N_2O at different temperatures, indicating that the role of the samarium was to transfer electrons to cobalt to stabilize/regenerate the active site.[47] Similarly, Zhang *et al.* looked at the impact of doping NiO with praseodymium and found that praseodymium increased the overall surface area of the catalyst and improved the conversion to reach 100% at ~400 °C (which is roughly the T_{50} of unpromoted NiO).[48] In addition, they found that with the addition of Pr, there were little differences in activity when placed in a feed with oxygen, which is typically an inhibiting gas. From XPS, these researchers observed that praseodymium helped weaken the nickel–oxygen bond, increasing the number of surface oxygens and promoting oxygen vacancies, as well as enhancing the reducibility of nickel. These factors are crucial for regenerating the active sites of the catalysts.[48] Other studies have found similar results when promoting Co_3O_4 catalysts with other lanthanides. Sun *et al.* promoted a Co_3O_4 catalyst with Ce and Pr.[49] They found that the Ce was imperative to aid in the formation of oxygen vacancies but overall restricted the formation of crystalline Co_3O_4. When Pr was doped into the catalyst, it added an electronic effect to further enhance the redox properties of the catalyst.[49] Dy has also been investigated as a promoter to Co_3O_4 catalysts.[50,51] As previously described, alkali metals, such as K, have been discovered as beneficial towards increasing decomposition activity due to having strong electron donating properties. However, studies have noted that in the presence of inhibiting gases, such as NO_x and CO_2, the role of K becomes inhibited. To further aid in decreasing the Co–O bond and strengthen the redox capabilities of the active species, Dy has been found to be an effective promoter.[50,51]

In addition, there have been various studies discussing further elements that can improve the activity of Co_3O_4 catalysts.[52–55] In short, Bi has been noted to create more active Co_3O_4 catalysts by increasing surface area and exposing more active crystal planes.[52] Other non-metal atoms, such as F and N have also been used as dopants to Co_3O_4 catalysts and are noted to promote the reaction by enhancing the surface basicity of the catalyst while creating more oxygen vacancies for the reactions to occur.[53,54]

High entropy oxides (HEOs) have been shown to exhibit unique properties beyond the sum of their constituent components and often outperform their mono- or bi-component counterparts. Recently, Li *et al.* explored a HEO spinel structure based on Co_3O_4 for N_2O decomposition.[57] The $(CuMgNiZn)_1Co_2O_4$ HEO outperformed Co_3O_4, as well as each bimetallic MCo_2O_4 (M = Cu, Mg, Ni, Zn). The HEO had a lower T_{50} (313 °C) and activation energy (89.6 kJ mol^{-1}) than the base Co_3O_4 (343 °C and 119.9 kJ mol^{-1}, respectively) and demonstrated a higher thermal stability over 12 h (Fig. 5C). The enhanced performance was attributed to the abundance of surface oxygen vacancies, caused by the lattice distortion due to multiple cation sizes. N_2O decomposition was also studied on a $La_{0.7}Ba_{0.3}Mn_{0.8}In_{0.2}O_3$ by Ishihara *et al.*[58] The base $LaMnO_3$ perovskite structure was modified by partial replacement of La and Mn with Ba and In, respectively, leading to a lower T_{50} value of 443 °C. While not a true HEO by definition, this complex oxide material highlights property enhancement based on cation substitution.

2.3 Zeolites

Zeolites have been extensively studied for their role in the decomposition reaction of N_2O. Specifically, zeolites can boost N_2O decomposition due to various characteristics, such as the increased surface area and structure giving rise to shape selectivity and control.[26] In addition, zeolites can support reactions due to their acidity.[25,26] Likewise, BEA and SSZ-13 have shown an additional benefit of hydrothermal stability, which is important for some processes that produce N_2O and contain water in the feed[24] (note: three-letter codes for zeolite structures are assigned by the International Zeolite Association[86]). Common zeolite structures for N_2O decomposition reactions are shown in Fig. 6A–D with labeled pore sizes.

Fe, Cu, and Co have been studied extensively for N_2O decomposition when exchanged into zeolites. Lin *et al.* analyzed Fe, Cu, and Co over a SSZ-13 zeolite and determined that the Fe-SSZ-13 catalyst had the largest decomposition rate when compared to the Co- and Cu-exchanged catalysts.[28] H_2-TPR and FTIR showed that the Fe-exchanged catalysts were found to have active dimeric [Fe–O–Fe] sites for decomposition, as well as Cu-exchanged catalysts having many dimeric Cu^{2+} sites to aid in the recombination of oxygen for the reaction mechanism.[28] The results indicate a dual site mechanism for both the Fe and Cu-based zeolites, compared to Co-exchanged zeolites, which displayed single Co^{2+} sites.[28] The authors related the apparent activity towards the trends in the activation energy, where the Fe-exchanged

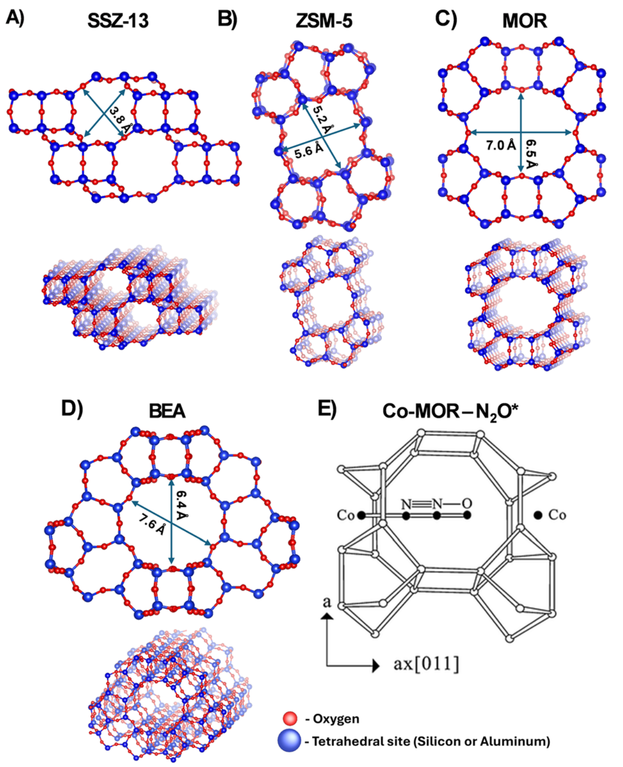

Fig. 6 (A–D) Structures for SSZ-13, ZSM-5, MOR, and BEA with associated pore sizes of commonly utilized zeolites for N_2O abatement reactions. Structural data from ref. 87–90, respectively. (E) Graphical representation of the interaction between N_2O and a β-type Co site of a Co-MOR zeolite. Reprinted from ref. 62 with permission from the Royal Society of Chemistry.

zeolites showed the lowest activation energy, corresponding to the highest reaction rate.

The formation of active sites depends on the interaction of metal ions with the zeolite framework. Zhang *et al.* analyzed how the structure of zeolites impacted the generation of Co active sites for N_2O decomposition.[62] The study analyzed Co, exchanged into ZSM-5, BEA, MOR, and USY zeolites and found that the activity (based on lowest T_{50} value to highest T_{50} value) followed: MOR > BEA ≈ ZSM-5 > USY, with a difference in T_{50} values of ~100 °C between the best and worst performing catalyst. The catalysts exhibited similar, yet slightly different, results when comparing activity in terms of turnover frequency (ZSM-5 > BEA > MOR > USY) but yielded a different result when comparing with Co loading (MOR > USY > BEA > ZSM-5). Not only could the differences be attributed to the type of zeolite, but the types of active sites as well as coordination to the framework were also found to be impactful. NO-FTIR (with NO used as a probe molecule), H_2-TPR, and UV-vis DRS (diffuse reflectance spectra) revealed that the more active catalysts (Co-ZSM-5, Co-MOR, and Co-BEA) had larger amounts of Co^{2+} sites compared to Co-USY, which had an increased amount of cobalt oxide.[62] It was found that an increase in Co concentration decreased the population of α-type Co^{2+} ions (Co^{2+} coordinated to four framework oxygens in the straight channel) and increased the β-type Co^{2+} ions (coordinated to more oxygens in the framework/cavity). This trend was evidenced more prominently in Co-BEA and Co-MOR when compared to Co-ZSM-5. The authors noted that the α-type sites for the ZSM-5 catalysts enable an increased interaction between the reactants and ions, with a decreased interaction between the ion and the framework, which attributed towards increased interactions with the reactants to facilitate decomposition. Similarly, they found that weaker bonds were formed between the Co^{2+} ion and the framework oxygens of the BEA zeolite in a β-type site, allowing the ions to coordinate with N_2O for the reaction despite having more diffusional hinderances due to zeolite structure. On the other hand, the Co ions exchanged into MOR in a β-type site exhibited increased bonding of the ion to the framework, which decreased the affinity of the bonds to N_2O. Though less accessible to bonding to the reactants, the authors noted that the structure within the MOR cavity locates Co^{2+} ions in close proximity with one another leading to the formation of ion pairs that can facilitate N_2O decomposition (Fig. 6E).[62]

Not only does the zeolite structure impact the reaction, but the ion exchange ratio and Si/Al ratio can impact the kinetics and mechanism of the reaction. Fanson *et al.* studied the Cu-ZSM-5 zeolite while analyzing the impact of the Si/Al ratio and Cu-exchange level on the kinetic rate oscillations for N_2O decomposition to understand surface reaction intermediates.[91] They found that higher Si/Al ratios resulted in kinetic rate oscillations. The authors attributed these oscillations to the formation and coverage of a nitrate species intermediate that formed due to the interaction of N_2O with the extra lattice oxygen in the zeolite. They concluded that the mechanism involves the conversion of N_2O to NO, which was shown to be rate determining step of this reaction on zeolites with a higher Si/Al ratio.[91]

Aside from the transition-metal exchanged zeolites, Sobalik *et al.* analyzed the impact of incorporating noble metals (Pt, Rh, and Ru) into Fe-FER zeolites.[63] It was found that when Fe and the noble metals were incorporated into the zeolite together, the T_{50} number decreased from ~420–450 °C for monometallic-FER zeolites to ~360–410 °C for bimetallic zeolites. In conducting isotopic experiments, the authors attributed this increased activity towards the ability of the noble metals to enhance recombination of the oxygen species that were bound to the surface and decreased the role of the oxygens from the framework of the zeolite.[63]

The role of the zeolite is also important in addition to the properties of the metals that allow for the reaction to occur. Guzmán-Vargas *et al.* synthesized Fe-exchange zeolites with BEA, FER, and ZSM-5 type zeolites.[64] Guzmán-Vargas *et al.* found the Fe-FER zeolite to be the most active with the lowest T_{50} (~417–437 °C) compared to the least active, which was the Fe-ZSM-5 (T_{50}: ~497–507 °C). The authors related this difference in activity towards the ability of the host zeolite to yield "oxo-species", where there is a cation in the species. They found through H_2-TPR that the Fe-FER catalysts were able to generate these species, which is indicative of the active iron complex for the reaction.[64] Wang *et al.* also analyzed how the influence of the host zeolite impacted the formation of the active centers and related it to the apparent N_2O decomposition activity.[24] In their study, they exchanged iron into both BEA and SSZ-13 zeolites. Based on UV-vis experiments, the authors found that the Fe-BEA zeolites had larger proportions of dimers and oligomeric iron-oxides as well as Fe_2O_3 particles, which are inactive. This aligns with their catalytic activity tests.[24]

The porosity of the zeolite can also impact the reaction. Lim *et al.* looked at a variety of Fe-exchanged small pore zeolites, and they found that the smaller pore zeolites, such as the H-Fe-PST-7, outperformed the medium-pore zeolites, such as the Fe-ZSM-5.[65] Similarly, Rutkowska *et al.* sought to increase the surface area by decreasing the micropore volume of zeolites by incorporating BEA to SBA-15.[26] When analyzing N_2 adsorption–desorption tests, they found that they were able to increase the mesoporosity of the zeolite while decreasing the micropore volume. When exchanging Fe into the catalysts, they found that there was an increase in Fe^{3+} centers when compared to the Fe-BEA catalysts, which had more Fe_2O_3 structures in the extra framework. Though there was an increase in iron-oxides in the Fe-BEA, these catalysts still had similar activity to the micro/mesoporous structures. The authors did note, however, that these micro/mesoporous zeolites had a lower iron loading, as found through UV-vis, thus indicating that the introduction of mesoporosity can boost activity.[26] Wu *et al.* also examined the value of adding mesopores to zeolites through alkaline treatment.[66] They found that with the alkaline treatment, the overall ion-exchange percentage increased between the parent zeolite and the modified zeolite, which correlated to a decrease in T_{50} (of between 50–100 °C) for all alkaline and parent zeolites.[66]

Furthermore, various *operando* studies have been conducted to elucidate the reaction mechanisms on Fe-zeolites. Cano-Blanco *et al.* performed a series of *operando* investigations on Fe-zeolites and discovered through *operando* diffuse reflectance UV-vis (DRUV) spectroscopy that N_2O decomposition on these materials is controlled by the reduction process in the redox mechanism, which was rate-limiting.[92] By coupling these findings with a series of other *operando* techniques, such as DRIFTS and electron paramagnetic resonance (EPR) spectroscopy, the researchers concluded that the Fe ions in the 6-membered rings playing a crucial role in the reaction mechanism. These Fe ions can complete the redox cycle necessary to regenerate active sites. *Operando* EPR studies further identified the Fe^{2+} species in the 6-membered ring of the zeolite as the active component for N_2O decomposition.[92]

2.4 Impact of inhibiting gases

The above three subsections focus on the direct decomposition activity of three main catalyst types in more "idealized" gas feeds, which may not be the actual operating conditions these catalysts may face in industrial applications. Many industrial processes, such as denitrification,[8] treatment of byproducts from ammonia combustion,[9] adipic acid production and nitric acid production,[12] as well as byproducts from three-way catalytic converters produce other byproducts, such NO_x, O_2, H_2O, and SO_2.[11] Many studies on direct decomposition catalysts show an inhibiting effect of NO, O_2, H_2O,[21] and SO_2.[43,46,93] Specifically, it has been noted in literature that NO, O_2, and H_2O have reversible inhibitory effects, indicating competitive adsorption/site blocking of the catalytic active sites.[31,94] Some literature has also suggested that NO decreases catalytic activity in that it has a competitive reaction pathway with labile oxygen in a CuO/CeO_2 catalyst.[21] SO_2 has also been found to negatively impact N_2O decomposition.[40,93] One study conducted a step change experiment in which various concentrations of SO_2 were added or removed while running the experiment for 8 h. It was found that SO_2 negatively impacted the performance with some irreversible deactivation in that the performance did not fully return to the initial activity once removing SO_2.[93] Studies suggest that the SO_2 is responsible for creating Brønsted acid sites on Pd/Al_2O_3 catalysts, which alters the oxidation state of the active material causing the irreversible deactivation.[40] For further catalytic improvement for such compounds, adding promoters or dopants can help facilitate the desorption and/or weaker binding of these inhibiting compounds, which creates a more robust catalyst under industrial conditions.[37,45,49–55] Yu *et al.* found that doping a Co_3O_4 catalyst with K and Dy improved the catalyst's performance and stability in environments containing NO, O_2 and H_2O.[51] In addition, the choice of support or oxide is important as it could reduce the negative impacts water and O_2 have on the N_2O decomposition.[93,95,96]

2.5 Direct decomposition catalyst durability

In addition to catalytic activity, catalyst durability is a critical property for the industrial application of direct decomposition and SCR of N_2O processes, especially under actual plant operating conditions.

The catalyst durability in the direct decomposition of N_2O has been investigated in literature, with some studies using industry-relevant feed stream and reaction conditions. Porous Fe_2O_3–ZrO_2 and NiO–ZrO_2 nanocomposites were tested for direct N_2O decomposition and showed a stable N_2O conversion at 500 °C for 120 hours.[97] In this case, the robust catalytic performance was attributed to the presence of reducible M–O–Zr (M = metal) interactive species and crystalline tetragonal ZrO_2 phase. Sádovská *et al.* studied the catalyst durability of Fe-FER, which is one of the highly active zeolite-based catalysts for N_2O decomposition.[98] The Fe-FER catalyst was exposed to a gas stream produced by NH_3 oxidation over Pt wire at 800 °C, which is the real conditions in the secondary stage of N_2O abatement during HNO_3 production, for 12 days. They found that the FER zeolite structure remained stable and the catalytic activity associated with Fe(II) cations for the N_2O decomposition was preserved after the catalyst aging under real process conditions. The excellent catalyst durability of Fe-FER compared to Fe-MFI under real conditions of nitric acid production plants was also discussed in other studies.[99,100] Melián-Cabrera *et al.* reported a stable N_2O conversion (~80%) for 50 hours at 427 °C with the presence of H_2O and O_2 in the feed stream, which was attributed to the stabilization of iron species in the FER matrix.[100] Giecko *et al.* studied the N_2O decomposition on Fe_2O_3/Al_2O_3 catalysts, which showed insignificant activity loss after 180 h time-on-stream in the pilot plant and 3300 h time-on-stream in the real nitric acid production plant.[101] In another study on the N_2O decomposition from adipic acid plant, Alini *et al.* found that $CaMn_{0.6}Cu_{0.4}O_3$ perovskite catalyst has good stability when tested under real industrial conditions at the temperature of 700–750 °C for 1400 hours using off-gas stream that contains H_2O, O_2, CO_2, and N_2O.[102] Wang *et al.* also tested a Co_3O_4 catalyst co-doped with Ni and Y and found it remained stable for 40 h with performance being attributed towards the promoters' role in enhancing O_2 desorption, increasing electron donation abilities of the active ions, increasing the basicity of the catalyst, as well as promoting the reduction of Co^{3+} to Co^{2+}.[55]

3 Selective catalytic reduction of nitrous oxide

In addition to the direct catalytic decomposition of N_2O, the SCR of N_2O has gained significant attention from the scientific community and industry alike.[103] The presence of reductants benefits the conversion of N_2O over different heterogeneous catalysts, as it lowers the reaction temperature required for reducing N_2O into inert nitrogen molecules. There are four main reductants that have been studied extensively in the literature for the SCR of N_2O processes and will be discussed in the following sections: CO, hydrocarbons, NH_3, and H_2. The catalytic performance of SCR catalysts, indicated by T_{50} values, under various reaction conditions are summarized in Table 2 and Fig. 2C. In general, it shows that iron-zeolites are the most studied catalysts for the SCR of N_2O, especially when NH_3 is used as the reductant. The reaction mechanisms and the influence of common industry-relevant impurity gases, such as NO, O_2, H_2O, and SO_2, on the SCR of N_2O are discussed in this section.

3.1 Carbon monoxide (CO-SCR)

CO has been considered an efficient and selective reductant for the conversion of N_2O. In general, CO can react with adsorbed oxygen and remove these atoms from the catalyst surface (also known as a scavenging effect), leading to a considerably decreased reaction temperature compared to the direct catalytic decomposition of N_2O.[69,70] There are two main reaction mechanisms of N_2O reduction by CO proposed in literature (*i.e.* the redox or associative routes) depending on the catalyst system.[60]

In the redox mechanism, N_2O first adsorbs to the surface, releasing reduced N_2, and leaving O adsorbed (eqn (6)). This is then followed by either the Langmuir–Hinshelwood mechanism (eqn (7) and (8)) or the Eley–Rideal mechanism (eqn (9)) to oxidize CO to CO_2. In the associative mechanism, simultaneous oxidation and reduction occurs by adsorbed CO (eqn (10)) reacting with either gaseous N_2O (eqn (11)) or adsorbed N_2O (eqn (12) and (13)):

Redox mechanism:

$$N_2O + * \rightarrow N_2 + O* \tag{6}$$

$$CO + * \rightarrow CO* \tag{7}$$

$$CO* + O* \rightarrow CO_2 + 2* \tag{8}$$

$$CO + O* \rightarrow CO_2 + * \tag{9}$$

Associative mechanism:

$$CO + * \rightarrow CO* \tag{10}$$

$$CO* + N_2O \rightarrow CO_2 + N_2 + * \tag{11}$$

$$N_2O + * \rightarrow N_2O* \tag{12}$$

$$CO* + N_2O* \rightarrow CO_2 + N_2 + 2* \tag{13}$$

Delahay *et al.* studied a variety of reductants for the SCR of N_2O over two Fe-BEA catalysts in the presence of oxygen.[67] It was found that CO is an effective reductant with an onset temperature of ~200 °C for N_2O reduction, which is lower than other reductants like propene and ammonia. Based on the superimposed curves of N_2O reduction by CO and N_2O decomposition on the reduced Fe-BEA at below 330 °C, the reoxidation of Fe^{2+} to Fe^{3+} species by N_2O was suggested to be the rate limiting step in the CO-SCR of N_2O in the low temperature region. In a study of CO-SCR of N_2O over Fe-ZSM-5 and Fe-silicalite, Pérez-Ramírez *et al.* reported that the reaction rate has a linear correlation with the CO/N_2O feed ratio (up to 1:1) and depends strongly on the catalyst preparation method.[69] They found the preparation method affects the distribution of iron species on the catalyst surface as well as the interaction of CO with iron sites which in turn accelerate N_2O removal. A site-dependent reaction mechanism was proposed by using *in situ* UV/vis and electron paramagnetic resonance (EPR) spectroscopy analyses. The authors concluded that while the reduction of N_2O by coordinated CO on Fe^{3+} ions can occur without changing oxidation states over isolated iron species, a redox Fe^{3+}/Fe^{2+} cycle with the formation of intermediate oxygen anion-radicals ($O\cdot^-$) happens over oligo-nuclear iron clusters. Wu *et al.* applied a multifaceted approach of experimental testing, catalyst characterization, and density functional theory (DFT)/*ab initio* molecular dynamics (AIMD) modeling to identify the catalytic role and transformation of different relevant iron species (mononuclear, binuclear, clusters, and Fe_2O_3 particles, see Fig. 7A) in Fe-ZSM-5 catalysts upon exposure to CO in the SCR of N_2O.[111] It was concluded that N_2O is activated on isolated iron sites to generate adsorbed oxygen species that then react with CO following the Eley–Rideal mechanism, while CO interacts with Fe_2O_3 particles to form oxygen vacancies that dissociate N_2O following the Mars–van Krevelen mechanism (Fig. 7B). It is worth noting that the Mars–van Krevelen mechanism was also proposed in CO-SCR of N_2O on phosphotungstic acid supported single-atom catalysts.[112] In this case, CO reductant is oxidized by the oxygen atom from the support to form an oxygen vacancy, which is replenished by N_2O to release N_2 into gas phase. Recently, advanced *in situ*/*operando* spectroscopy approach was utilized to study the reduction and oxidation half cycles of CO-SCR of N_2O over Fe-zeolites.[113,114] Qian *et al.* investigated the redox cycle of Fe-BEA catalyst during the CO-SCR of N_2O in an excess oxygen environment by *operando*/*in situ* diffuse reflectance ultraviolet-visible (UV-vis) spectroscopy and *in situ* Fe K-edge X-ray absorption (XAS) spectroscopy.[113] Based on the *operando* UV-vis and XAS results, the redox cycle of Fe active sites was proposed in two steps: (i) Fe^{III}-α-O species are reduced by CO to generate Fe^{II} species and CO_2; (ii) Fe^{II} active sites reduce N_2O to form N_2 and regenerate Fe^{III}-α-O species. Quantitative spectro-kinetic analysis revealed a higher reactivity of Fe^{II} sites with N_2O compared to O_2, enabling a selective CO + N_2O reaction under excess O_2 conditions. Fischer *et al.* examined the redox

Table 2 Summary of N_2O SCR catalysts, grouped by reductant from top to bottom: CO, hydrocarbons, NH_3, and H_2. T_{50} represents the temperature at which 50% conversion is reached, with flow conditions being defined by the gas hourly space velocity (GHSV), weight hourly space velocity (WHSV), or ratio of catalyst weight to volumetric gas flow rate (*W*/*F*). Note: GHSV, WHSV, and *W*/*F* were standardized based on feed conditions presented in the literature source for further comparison

Reductants	Other reactants[a]	Inhibitors[b]	Catalyst	Catalyst synthesis	Catalyst pretreatment	GHSV (h^{-1})	WHSV (h^{-1})	*W*/*F* (g s mL^{-1})	Feed composition	T_{50} (°C)	Ref.
CO			$Pt/Al_2O_3–CeO_2–La_2O_3$	Co-precipitation, impregnation	H_2/He, 400 °C, 1 h followed by He, 400 °C, 1 h	10 000			0.1% N_2O, 0.1% CO, He balance	239	38
CO		O_2	$Pt/Al_2O_3–CeO_2–La_2O_3$	Co-precipitation, impregnation	H_2/He, 400 °C, 1 h followed by He, 400 °C, 1 h	10 000			0.1% N_2O, 0.1% CO, 2% O_2, He balance	427	38
CO			Al–Pd–Co–O mixed oxide	Co-precipitation of hydrotalcite-type precursors		30 000			12 500 ppm N_2O, 17 500 ppm CO, N_2 balance	133	61
CO			Al–Rh–Co–O mixed oxide	Co-precipitation of hydrotalcite-type precursors		30 000			12 500 ppm N_2O, 17 500 ppm CO, N_2 balance	160	61
CO			Co–Rh–Al–O mixed oxide	Co-precipitation of hydrotalcite-type precursors	N_2, 500 °C, >3 h	30 000			12 500 ppm N_2O, 17 500 ppm CO, N_2 balance	173	59
CO			Co–Pd–Al–O mixed oxide	Co-precipitation of hydrotalcite-type precursors	N_2, 500 °C, >3 h	30 000			12 500 ppm N_2O, 17 500 ppm CO, N_2 balance	174	59
CO		NO	Al–Pd–Co–O mixed oxide	Co-precipitation of hydrotalcite-type precursors		30 000			12 500 ppm N_2O, 17 500 ppm CO, 100 ppm NO, N_2 balance	256	61
CO			Co–Mn–Al–O mixed oxide	Co-precipitation of hydrotalcite-type precursors	He, 450 °C, 1 h		10.9		0.1 mol% N_2O, 0.15 mol% CO, He balance	297	60
CO		O_2	Co–Mn–Al–O mixed oxide	Co-precipitation of hydrotalcite-type precursors	He, 450 °C, 1 h		10.9		0.1 mol% N_2O, 0.15 mol% CO, 20 mol% O_2, He balance	447	60
CO		O_2	Co–Pd–Al–O mixed oxide	Co-precipitation of hydrotalcite-type precursors	N_2, 500 °C, >3 h	30 000			12 500 ppm N_2O, 17 500 ppm CO, 10 500 ppm O_2, N_2 balance	460	59
CO			Fe/ZSM-5	Sublimation	N_2O/He, 450 °C, 1 h		10.9		N_2O (1.5 mbar) and CO (0.3–1.5 mbar), He balance	298–458	69
CO			Fe-ZSM-5	Ion exchange	O_2, 500 °C, 1 h		9.9		1000 ppm N_2O, 1000 ppm CO, He balance	306–460	104
CO			Fe/silicalite	Isomorphous substitution, ion exchange, steam activation	N_2O/CO/He, 450 °C, 1 h		11.3		N_2O (1.5 mbar), CO (1 mbar), He balance	362	68
CO			Fe/ZSM-5	Isomorphous	He, 450 °C, 2 h	90 000			N_2O (1.5 mbar),	362–507	70

Table 2 *(continued)*

Reductants	Other reactants[a]	Inhibitors[b]	Catalyst	Catalyst synthesis	Catalyst pretreatment	GHSV (h^{-1})	WHSV (h^{-1})	*W*/*F* (g s mL^{-1})	Feed composition	T_{50} (°C)	Ref.
				substitution, ion exchange, steam activation					CO (0.2–3.0 mbar), He balance		
CO	O_2		Fe-BEA	Ion exchange	3% H_2/Ar, 13 mL min^{-1}, ramp from 80–700 °C at 10 °C min^{-1}	35 000			0.2% N_2O, 0.2% CO, 3% O_2, He balance	369–377	67
CO			Fe-USY	Ion exchange	He, 600 °C, 1 h	30 000			5000 ppm N_2O, 5000 ppm CO, He balance	372	72
CO	O_2		Fe-USY	Ion exchange	He, 600 °C, 1 h	30 000			5000 ppm N_2O, 5000 ppm CO, 50 000 ppm O_2, He balance	372	72
CO			Fe/ZSM-5	Isomorphous substitution, ion exchange, steam activation	He, 450 °C, 2 h	90 000			N_2O (1.5 mbar), CO (0.2–1.5 mbar), He balance	381–509	71
CO			Fe/ZSM-5	Isomorphous substitution, steam activation	N_2O/He, 450 °C, 1 h		10.9		N_2O (1.5 mbar) and CO (0.3–1.5 mbar), He balance	385–495	69
CO			Fe/ZSM-5	Isomorphous substitution, ion exchange, steam activation	N_2O/CO/He, 450 °C, 1 h		11.3		N_2O (1.5 mbar), CO (1 mbar), He balance	408	68
CO	NO		Fe/ZSM-5	Isomorphous substitution, ion exchange, steam activation	He, 450 °C, 2 h	90 000			N_2O (1.5 mbar), CO (1.5 mbar), NO (1.5 mbar), He balance	413	70
CH_4			Pd/Al_2O_3	Dry impregnation	He, 100 mL min^{-1}, 600 °C, 1 h	35 000			0.12% N_2O, 0.5% CH_4, He balance	258	40
C_3H_6			Rh/Al_2O_3	Dry impregnation				0.12	500 ppm N_2O, 1000 ppm C_3H_6, He balance	292	39
C_3H_6			$Pt/Al_2O_3–CeO_2–La_2O_3$	Co-precipitation, impregnation	H_2/He, 400 °C, 1 h followed by He, 400 °C, 1 h	10 000			0.1% N_2O, 0.1% C_3H_6, He balance	317	38
CH_4		O_2	Pd/Al_2O_3	Dry impregnation	He, 100 mL min^{-1}, 600 °C, 1 h	35 000			0.12% N_2O, 0.5% CH_4, 5% O_2, He balance	331	40
CH_4		SO_2	Pd/Al_2O_3	Dry impregnation	He, 100 mL min^{-1}, 600 °C, 1 h	35 000			0.12% N_2O, 0.5% CH_4, 300 ppm SO_2, He balance	355–462	40
CH_4		H_2O	Pd/Al_2O_3	Dry impregnation	He, 100 mL min^{-1}, 600 °C, 1 h	35 000			0.12% N_2O, 0.5% CH_4, 3% H_2O, He balance	376–414	40
C_3H_6	O_2		Rh/Al_2O_3	Dry impregnation				0.12	500 ppm N_2O, 1000 ppm C_3H_6, 5% O_2, He balance	392	39
C_3H_6	O_2	SO_2	Rh/Al_2O_3	Dry impregnation				0.12	500 ppm N_2O, 1000 ppm C_3H_6, 5% O_2, 50 ppm SO_2, He balance	403	39
C_3H_6	O_2		Ru/Al_2O_3	Dry impregnation				0.12	500 ppm N_2O, 1000 ppm C_3H_6, 5% O_2, He balance	413	39
C_3H_6	O_2	H_2O	Rh/Al_2O_3	Dry impregnation				0.12	500 ppm N_2O, 1000 ppm C_3H_6, 5% O_2, 10% H_2O, He balance	419	39
C_3H_6	O_2	SO_2	Ru/Al_2O_3	Dry impregnation				0.12	500 ppm N_2O, 1000 ppm C_3H_6, 5% O_2, 50 ppm SO_2, He balance	420	39

Table 2 *(continued)*

Reductants	Other reactants[a]	Inhibitors[b]	Catalyst	Catalyst synthesis	Catalyst pretreatment	GHSV (h^{-1})	WHSV (h^{-1})	*W*/*F* (g s mL^{-1})	Feed composition	T_{50} (°C)	Ref.
C_3H_6	O_2	H_2O	Ru/Al_2O_3	Dry impregnation				0.12	500 ppm N_2O, 1000 ppm C_3H_6, 5% O_2, 10% H_2O, He balance	450	39
C_3H_6		O_2	$Pt/Al_2O_3–CeO_2–La_2O_3$	Co-precipitation, impregnation	H_2/He, 400 °C, 1 h followed by He, 400 °C, 1 h	10 000			0.1% N_2O, 0.1% C_3H_6, 2% O_2, He balance	454	38
C_3H_6			Ru/Al_2O_3	Dry impregnation				0.12	500 ppm N_2O, 1000 ppm C_3H_6, He balance	485	39
C_3H_8	O_2		Fe/ZSM-5	Solid state ion exchange	He, 500 °C	7500			1000 ppm N_2O, 1000 ppm C_3H_8, 4% O_2, He balance	279	105
CH_4			Fe-ZSM-5	Ion exchange	O_2, 500 °C, 1 h		9.9		950 ppm N_2O, 500 ppm CH_4, He balance	290–395	104
C_3H_8		O_2, H_2O	Pd–Fe/ZSM-5	Ion exchange, incipient wetness impregnation	N_2, 175 °C, 2 h	20 000			1900 ppm C_3H_8, 1500 ppm N_2O, 100 ppm NO, 100 ppm NO_2, 0.5% H_2O, 2.5% O_2, N_2 balance	304	106
C_3H_8	O_2		Fe/silicalite	Isomorphous substitution, ion exchange, steam activation	$N_2O/C_3H_8/O_2$/He, 450 °C, 1 h		11.3		N_2O (1.5 mbar), C_3H_8 (1.5 mbar), He balance	330	68
C_2H_6	O_2		Fe/ZSM-5	Isomorphous substitution, ion exchange, steam activation	O_2/He, 450 °C, 1 h	60 000			N_2O (1.5 mbar), C_2H_6 (0.44 mbar), O_2 (20 mbar), He balance	332	107
C_3H_8	O_2	H_2O	Fe/ZSM-5	Solid state ion exchange	He, 500 °C	7500			1000 ppm N_2O, 1000 ppm C_3H_8, 7% H_2O, 4% O_2, He balance	332	105
CH_4	O_2		Fe/ZSM-5	Isomorphous substitution, ion exchange, steam activation	O_2/He, 450 °C, 1 h	60 000			N_2O (1.5 mbar), CH_4 (0.93 mbar), O_2 (20 mbar), He balance	337	107
CH_4	O_2		Fe-ZSM-5	Ion exchange	O_2, 500 °C, 1 h		9.9		950 ppm N_2O, 500 ppm CH_4, 10% O_2, He balance	338–470	104
CH_4			Fe-USY	Ion exchange	He, 600 °C, 1 h	30 000			5000 ppm N_2O, 2000 ppm CH_4, He balance	344	72
n-$C_{10}H_{22}$	O_2		Fe-BEA	Ion exchange	3% H_2/Ar, 13 mL min^{-1}, ramp from 80–700 °C at 10 °C min^{-1}	35 000			0.2% N_2O, 0.03% *n*-$C_{10}H_{22}$, 3% O_2, He balance	346–377	67
C_2H_6	O_2	NO	Fe/ZSM-5	Isomorphous substitution, ion exchange, steam activation	O_2/He, 450 °C, 1 h	60 000			N_2O (1.5 mbar), C_2H_6 (0.44 mbar), NO (0.13 mbar), O_2 (20 mbar), He balance	347	107
CH_4		O_2, H_2O	Pd–Fe/ZSM-5	Ion exchange, incipient wetness impregnation	N_2, 175 °C, 2 h	20 000			4500 ppm CH_4, 1500 ppm N_2O, 100 ppm NO, 100 ppm NO_2, 0.5% H_2O, 2.5% O_2, N_2 balance	351	106
CH_4		O_2	Fe-USY	Ion exchange	He, 600 °C, 1 h	30 000			5000 ppm N_2O, 2000 ppm CH_4, 50 000 ppm O_2, He balance	352	72
C_3H_8	O_2		Fe/ZSM-5	Isomorphous substitution, ion exchange, steam activation	$N_2O/C_3H_8/O_2$/He, 450 °C, 1 h		11.3		N_2O (1.5 mbar), C_3H_8 (1.5 mbar), He balance	357	68

Table 2 *(continued)*

Reductants	Other reactants[a]	Inhibitors[b]	Catalyst	Catalyst synthesis	Catalyst pretreatment	GHSV (h^{-1})	WHSV (h^{-1})	W/F (g s mL^{-1})	Feed composition	T_{50} (°C)	Ref.
C_3H_8	O_2	NO	Fe/ZSM-5	Solid state ion exchange	He, 500 °C	7500			1000 ppm N_2O, 1000 ppm C_3H_8, 1000 ppm NO, 4% O_2, He balance	357	105
C_3H_8	O_2		Fe/ZSM-5	Isomorphous substitution, ion exchange, steam activation	$N_2O/C_3H_8/O_2$/He, 450 °C, 1 h	60 000			N_2O (1.5 mbar), O_2 (50 mbar), C_3H_8 (1.5 mbar), He balance	357	108
C_3H_6	O_2		Fe-BEA	Ion exchange	3% H_2/Ar, 13 mL min^{-1}, ramp from 80–700 °C at 10 °C	35 000			0.2% N_2O, 0.1% C_3H_6, 3% O_2, He balance	369–392	67
C_3H_8	O_2	NO	Fe/ZSM-5	Isomorphous substitution, ion exchange, steam activation	$N_2O/C_3H_8/O_2$/NO/He, 450 °C, 1 h	60 000			N_2O (1.5 mbar), O_2 (50 mbar), C_3H_8 (1.5 mbar), NO (4.5 mbar), He balance	384	108
CH_4		H_2O	Fe-USY	Ion exchange	He, 600 °C, 1 h	30 000			GHSV = 30 000 h^{-1}, 5000 ppm N_2O, 2000 ppm CH_4, 2% H_2O, He balance	385	72
C_2H_6	O_2	NH_3	Fe/ZSM-5	Isomorphous substitution, ion exchange, steam activation	O_2/He, 450 °C, 1 h	60 000			N_2O (1.5 mbar), C_2H_6 (0.44 mbar), NH_3 (1.1 mbar of NH_3), O_2 (20 mbar), He balance	388	107
CH_4		NO	Fe-USY	Ion exchange	He, 600 °C, 1 h	30 000			5000 ppm N_2O, 2000 ppm CH_4, 700 ppm NO, He balance	396	72
CH_4	O_2	NH_3	Fe/ZSM-5	Isomorphous substitution, ion exchange, steam activation	O_2/He, 450 °C, 1 h	60 000			N_2O (1.5 mbar), CH_4 (0.93 mbar), NH_3 (1.1 mbar of NH_3), O_2 (20 mbar), He balance	397	107
CH_4	O_2	NO	Fe/ZSM-5	Isomorphous substitution, ion exchange, steam activation	O_2/He, 450 °C, 1 h	60 000			N_2O (1.5 mbar), CH_4 (0.93 mbar), NO (0.13 mbar), O_2 (20 mbar), He balance	421	107
NH_3			RuO_2	Bulk oxide	He, 400 °C, 1 h		5.5		N_2O (1.5 mbar), NH_3 (1.5 mbar), He balance	256	56
NH_3	O_2		RuO_2	Bulk oxide	He, 400 °C, 1 h		5.5		N_2O (1.5 mbar), NH_3 (1.5 mbar), O_2 (1.5 mbar), He balance	345	56
NH_3			Rh-FAU	Wet impregnation	Air, 500 °C	30 000			0.2% N_2O, 0.2% NH_3, He balance	272	75
NH_3	O_2		Fe-BEA	Ion exchange		50 000			1000 ppm N_2O, 1500 ppm NH_3, 8% O_2, Ar balance	295	109
NH_3	O_2		Fe-ZSM-5	Ion exchange		50 000			1000 ppm N_2O, 1500 ppm NH_3, 8% O_2, Ar balance	310	109
NH_3	O_2, NO		Fe-FER	Ion exchange	Air, 50 mL min^{-1}, 550 °C, 2 h	200 000			$N_2O/NO/O_2/NH_3$/He = 0.1/0.15/3.0/0.25/96.5	327	64
NH_3			Fe-MOR	Ion exchange	He, 600 °C, 1 h	30 000			5000 ppm N_2O, 4000 ppm NH_3, He balance	367	73
NH_3	O_2		Fe-MOR	Ion exchange	He, 600 °C, 1 h	30 000			5000 ppm N_2O, 4000 ppm NH_3, 50 000 ppm O_2, He balance	367	73
NH_3	O_2		Fe-MOR	Ion exchange	He, 600 °C, 1 h	30 000			5000 ppm N_2O, 4000 ppm NH_3, 50 000 ppm O_2, He balance	367	74
NH_3	O_2		Fe-FAU	Ion exchange		50 000			1000 ppm N_2O, 1500 ppm NH_3,	370	109

Table 2 *(continued)*

Reductants	Other reactants[a]	Inhibitors[b]	Catalyst	Catalyst synthesis	Catalyst pretreatment	GHSV (h^{-1})	WHSV (h^{-1})	*W*/*F* (g s mL^{-1})	Feed composition	T_{50} (°C)	Ref.
									8% O_2, Ar balance		
NH_3			Fe-MOR	Ion exchange	He, 600 °C, 1 h	30 000			5000 ppm N_2O, 4000 ppm NH_3, He balance	374	74
NH_3	O_2		Fe-BEA	Ion exchange	3% H_2/Ar, 13 mL min^{-1}, ramp from 80–700 °C at 10 °C min^{-1}	35 000			0.2% N_2O, 0.2% NH_3, 3% O_2	374–397	67
NH_3	H_2O		Fe-BEA	Ion exchange	O_2/N_2, 500 °C, 1 h	200 000			540 ppm N_2O, 360 ppm NH_3, 2.5% H_2O, N_2 balance	389	24
NH_3			Fe-BEA	Ion exchange	He, 600 °C, 1 h	30 000			5000 ppm N_2O, 4000 ppm NH_3, He balance	397	73
NH_3	O_2		Fe-ZSM-5	Ion exchange	He, 600 °C, 1 h	30 000			5000 ppm N_2O, 4000 ppm NH_3, 50 000 ppm O_2, He balance	397	73
NH_3	O_2		Fe-ZSM-35	Ion exchange		50 000			1000 ppm N_2O, 1500 ppm NH_3, 8% O_2, Ar balance	400	109
NH_3			Fe-USY	Ion exchange	He, 600 °C, 1 h	30 000			5000 ppm N_2O, 4000 ppm NH_3, He balance	402	72
NH_3			Fe-USY	Ion exchange	He, 600 °C, 1 h	30 000			5000 ppm N_2O, 4000 ppm NH_3, He balance	407	73
NH_3	O_2		Fe-BEA	Ion exchange	He, 600 °C, 1 h	30 000			5000 ppm N_2O, 4000 ppm NH_3, 50 000 ppm O_2, He balance	407	73
NH_3			Fe-ZSM-5	Ion exchange	He, 600 °C, 1 h	30 000			5000 ppm N_2O, 4000 ppm NH_3, He balance	417	73
NH_3	O_2		Fe-FER	Ion exchange	Air, 50 mL min^{-1}, 550 °C, 2 h	35 000			$N_2O/O_2/NH_3/He = 0.2/3.0/0.2/96.6$	417	64
NH_3	H_2O	O_2	Fe-BEA	Ion exchange	O_2/N_2, 500 °C, 1 h	200 000			540 ppm N_2O, 360 ppm NH_3, 2.5% H_2O, 14% O_2, N_2 balance	426	24
NH_3	H_2O		Fe-SSZ-13	Ion exchange	O_2/N_2, 500 °C, 1 h	200 000			540 ppm N_2O, 360 ppm NH_3, 2.5% H_2O, N_2 balance	429	24
NH_3		O_2	Fe-USY	Ion exchange	He, 600 °C, 1 h	30 000			5000 ppm N_2O, 4000 ppm NH_3, 50 000 ppm O_2, He balance	430	72
NH_3	O_2		Fe-MCM-22	Ion exchange		50 000			1000 ppm N_2O, 1500 ppm NH_3, 8% O_2, Ar balance	435	109
NH_3	O_2		Fe-USY	Ion exchange	He, 600 °C, 1 h	30 000			5000 ppm N_2O, 4000 ppm NH_3, 50 000 ppm O_2, He balance	437	73
NH_3	O_2		Fe-SSZ-13	Ion exchange		50 000			1000 ppm N_2O, 1500 ppm NH_3, 8% O_2, Ar balance	450	109
NH_3	H_2O	O_2	Fe-SSZ-13	Ion exchange	O_2/N_2, 500 °C, 1 h	200 000			540 ppm N_2O, 360 ppm NH_3, 2.5% H_2O, 14% O_2, N_2 balance	455	24
NH_3		O_2	Rh-FAU	Wet impregnation	Air, 500 °C	30 000			0.2% N_2O, 0.2% NH_3, 3% O_2, He balance	487	75
H_2			Ni–Pt/SiO_2	Incipient wetness impregnation	H_2, 400 °C, 1 h	25 000			1250 ppm N_2O, 1250 ppm H_2, He balance	27–62	41
H_2			Pt/SiO_2	Incipient wetness impregnation	H_2, 400 °C, 1 h	25 000			1250 ppm N_2O, 1250 ppm H_2, He balance	122	41
H_2			Ni/SiO_2	Incipient wetness impregnation	H_2, 400 °C, 1 h	25 000			1250 ppm N_2O, 1250 ppm H_2, He balance	527	41

Table 2 *(continued)*

Reductants	Other reactants[a]	Inhibitors[b]	Catalyst	Catalyst synthesis	Catalyst pretreatment	GHSV (h^{-1})	WHSV (h^{-1})	W/F (g s mL^{-1})	Feed composition	T_{50} (°C)	Ref.
H_2			$Ti_{0.99}Pd_{0.01}O_{2-\delta}$	Solution combustion		43 000			$N_2O:H_2 = 1:3$ vol%, He balance	52	110
H_2			$Ti_{0.99}Rh_{0.01}O_{2-\delta}$	Solution combustion		43 000			$N_2O:H_2 = 1:3$ vol%, He balance	93	110
H_2			$Ti_{0.99}Pt_{0.01}O_{2-\delta}$	Solution combustion		43 000			$N_2O:H_2 = 1:3$ vol%, He balance	107	110
H_2			$Ti_{0.99}Ru_{0.01}O_{2-\delta}$	Solution combustion		43 000			$N_2O:H_2 = 1:3$ vol%, He balance	129	110
H_2			RuO_2	Bulk oxide	He, 400 °C, 1 h		5.5		N_2O (1.5 mbar), H_2 (1.5 mbar), He balance	216	56
H_2			RuO_2	Bulk oxide	H_2/He, 400 °C, 1 h		5.5		N_2O (1.5 mbar), H_2 (1.5 mbar), He balance	305	56
H_2	O_2		RuO_2	Bulk oxide	He, 400 °C, 1 h		5.5		N_2O (1.5 mbar), H_2 (1.5 mbar), O_2 (1.5 mbar), He balance	345	56
H_2	O_2		Fe-BEA	Ion exchange	3% H_2/Ar, 13 mL min^{-1}, ramp from 80–700 °C at 10 °C min^{-1}	35 000			0.2% N_2O, 0.2% H_2, 3% O_2	497–504	67

[a] Other reactants – present in the feed but do not inhibit N_2O conversion. [b] Inhibitors – present in the feed and inhibit N_2O conversion.

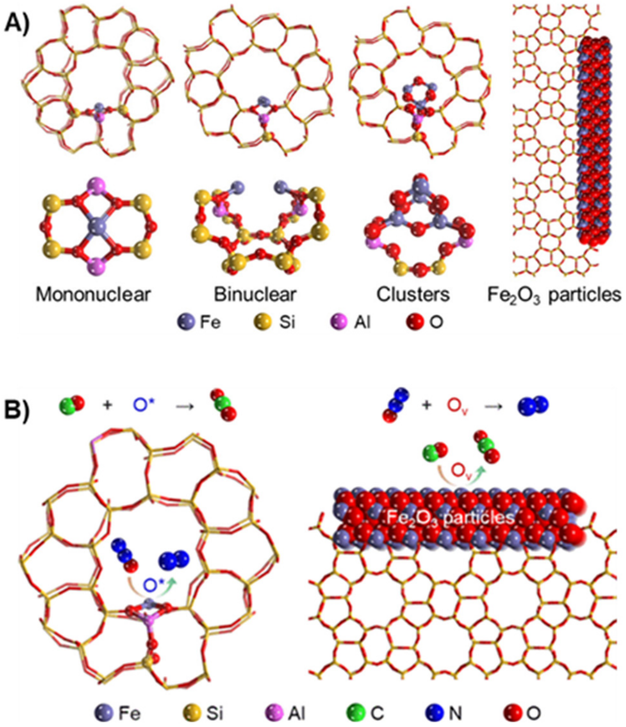

Fig. 7 (A) Schematic illustration of the different iron species in Fe/ZSM-5. (B) Proposed mechanisms of the SCR of N_2O by CO on isolated iron sites and Fe_2O_3 particles. Reprinted from ref. 111 with permission from the American Chemical Society.

kinetics in the CO-SCR of N_2O over Fe-FER by combining modulation excitation with *operando* electron paramagnetic resonance (EPR) spectroscopy.[114] They found that isolated Fe^{II} species in β-cationic positions are the only active sites during the reaction by enabling reversible Fe^{II}/Fe^{III} cycles, while isolated Fe^{II} sites in γ-cationic positions and oligomeric Fe species are spectator species.

Single atom catalysts have attracted increasing attention in recent years due to their superior catalytic performance and efficient atomic utilization. Khan *et al.* examined the reduction of N_2O in the presence of CO over metal-free Si-coordinated phthalocyanine catalyst by DFT calculations.[115] They found that the Si atom is energetically stabilized on the phthalocyanine support and can act as the active site for the N_2O dissociation. In another study, Ragab *et al.* employed DFT method to investigate aluminum-decorated $C_{24}N_{24}$ fullerene catalyst for the N_2O reduction in the presence of CO and O_2.[116] This single-atom catalyst exhibited a relatively low energy barrier and strong N_2O binding, minimizing the potential inhibition by CO and O_2 due to the competitive adsorption.

The presence of other gas molecules in the feed such as NO, oxygen, and water, which are commonly found in the nitric acid production tail gas, can affect the CO-SCR of N_2O over Fe-zeolites. This is clearly shown by the shift of T_{50} values with adding impurity gases to the feed stream on the same catalyst system (Table 2). N_2O decomposition can be assisted by addition of NO to facilitate oxygen desorption *via* adsorbed NO_2^- intermediates over oligo-nuclear iron species, however, CO-SCR of N_2O was inhibited by strong adsorption of NO on isolated iron sites in Fe-ZSM-5, especially at the low temperature regime.[70] This inhibitory effect of NO on CO-SCR of N_2O becomes less significant at high temperatures due to weaker adsorption of NO on iron active sites. Conversely, Wu *et al.* found that the addition of oxygen in the reactant feed showed an inhibitory effect on CO-SCR of N_2O over Fe-ZSM-5, which is attributed to the reaction between CO and O_2.[111] The presence of water exhibited a more negative effect than oxygen for this system.

While iron supported on zeolites are the most common catalysts for CO-SCR of N_2O, a few studies were conducted on noble metals (*i.e.*, Pt/Al_2O_3, Pd/Al_2O_3, or Rh/Al_2O_3) and mixed oxides (*i.e.*, Co–Rh–Al–O, Co–Pd–Al–O, or Co–Pd–Ce–Al–O).[60,61,117–119] Konsolakis *et al.* investigated rare earth oxide-modified $Pt/Al_2O_3–CeO_2$ and $Pt/Al_2O_3–CeO_2–La_2O_3$ structured catalysts (*i.e.* coated on ceramic honeycomb monoliths) in the absence and presence of excess oxygen and water.[117] Like the Fe-zeolites, reducing agents such as CO significantly improve N_2O conversion by aiding in the removal of strongly adsorbed oxygen species. In addition, oxygen and water have a detrimental effect on N_2O conversion, which were attributed to competitive adsorption and irreversible changes in platinum oxidation state. In another study on the role of rare-earth oxides promoters, Holles *et al.* found that ceria improves CO-SCR of N_2O on Pd/Al_2O_3 and Rh/Al_2O_3 due to additional storage sites for dissociated oxygen atoms and high reducibility, while La_2O_3 hinders the reaction due to lower metal dispersion.[119] The positive effect of adding CO as a reductant on the conversion of N_2O was reported for reactions over metal oxides (Co–Rh–Al, Co–Pd–Al, Co–Pd–Ce–Al) prepared by co-precipitation of hydrotalcite-type precursors.[59–61] They found that the presence of oxygen inhibits N_2O conversion over metal oxides, and NO showed an insignificant influence.

3.2 Hydrocarbons (HC-SCR)

The presence of hydrocarbons in the SCR of N_2O over iron zeolites has been studied extensively in literature and applied in commercial NO_x–N_2O abatement processes.[107] Hydrocarbons are selective reductants and effective for the reduction of N_2O over Fe-BEA catalysts.[67] The reaction mechanism of N_2O reduction by C_3H_6 over noble metals supported on alumina and by C_3H_8 over Fe-zeolites was proposed to be related to the removal of adsorbed atomic oxygen species by these hydrocarbons to form CO and CO_2.[39,108] Deeper investigations on CH_4-SCR reaction mechanism combining infrared spectroscopy and catalytic reaction tests over Fe-ZSM-5 and Fe-BEA indicated an interaction of methane and N_2O molecules on iron hydroxyl groups with the sequential oxidation to methoxy and formate intermediate species (eqn (14)–(17)):[72,120,121]

$$\text{Fe–OH} + CH_4 + N_2O \rightarrow \text{Fe–OCH}_3 + H_2O + N_2 \tag{14}$$

$$\text{Fe–OCH}_3 + 2\ N_2O \rightarrow \text{Fe–OOCH} + H_2O + 2\ N_2 \tag{15}$$

$$\text{Fe–OOCH} + N_2O \rightarrow \text{Fe–OH} + CO_2 + N_2 \tag{16}$$

$$\text{Overall: } 4\ N_2O + CH_4 \rightarrow CO_2 + 4\ N_2 + 2\ H_2O \tag{17}$$

A minor amount of CO detected in product streams may indicate the presence of an additional pathway with incomplete oxidation of CH_4 (eqn (14), (18) and (19)):[72,120,121]

$$\text{Fe–OCH}_3 + 2\ N_2O \rightarrow \text{Fe–OH} + CO + H_2O + 2\ N_2 \tag{18}$$

$$\text{Overall: } 3\ N_2O + CH_4 \rightarrow CO + 3\ N_2 + 2\ H_2O \tag{19}$$

Hevia *et al.* studied light hydrocarbons (C_1–C_3) with different degrees of unsaturation and proposed a set of criteria to optimally select hydrocarbons for SCR of N_2O over Fe-ZSM-5 zeolites, including N_2O reduction activity and operation temperature, hydrocarbon utilization or the selectivity to react with N_2O in O_2 excess, CO and CO_2 formation, sensitivity to NO and NH_3, and cost.[107] It was found that ethane and methane are the most effective reductants, while alkenes and alkynes require a higher temperature to consume O* and are less effective due to undesired non-selective reaction with oxygen. Nobukawa *et al.* similarly investigated the SCR of N_2O on Fe-ZSM-5 and found that methane is a more efficient reductant compared to higher alkanes (ethane and propane), hydrogen, and CO.[104] H_2-TPR and extended X-ray absorption fine structure analyses were performed to show that the high N_2O reduction activity at high Fe/Al ratio in Fe-ZSM-5 catalysts is likely due to the presence of binuclear iron species. In addition, the redox cycle of these active iron sites is promoted by the formation of methoxy species, which originated from the interaction of methane with N_2O-derived adsorbed oxygen. Conversely, Van den Brink *et al.* reported that propane is more active than methane in the SCR of N_2O over palladium-promoted Fe-ZSM-5 in the same temperature range of 200–500 °C.[106] The presence of water in the feed stream was found to be detrimental to the catalytic performance of N_2O reduction by propane over Fe-ZSM-5 catalysts.[105,106] A more significant inhibitory effect of NO on the reduction of N_2O by hydrocarbons was observed over different iron zeolite frameworks (Fe-ZSM-5, Fe-BEA, Fe-USY), which was ascribed to the competitive adsorption for iron active sites.[72,105,108] In addition to water and NO, oxygen also exhibited an adverse effect on the HC-SCR of N_2O, which was mainly attributed to competitive adsorption and non-selective oxidation of hydrocarbon intermediates to form CO.[72] As a result, they proposed that N_2O conversion in a mixed N_2O, CH_4, NO stream can be a combination of three pathways: CH_4-SCR, CO-SCR, and NO-assisted direct decomposition.

Regarding the catalytic iron species, Pérez-Ramírez *et al.* proposed that isolated extra-framework iron sites play an important role in in the reduction of N_2O by propane,[108] which was further verified by comparing steam-activated samples of Fe-silicalite and Fe-ZSM-5.[68] By employing UV-vis diffuse reflectance spectroscopy (DRS), it was revealed that isolated iron species dominate, steam-activated Fe/silicalite gave higher activity over the steam-activated Fe/ZSM-5 containing iron clustered species. However, the presence of iron clusters may be beneficial for the direct N_2O decomposition, as oxygen recombination is the rate limiting step. In addition, this comparison of Fe-silicalite and Fe-ZSM-5 implies a minor role of acid sites in the hydrocarbon-assisted reduction of N_2O. Another study by Debbagh *et al.* reported that the reduction of N_2O by methane and CO over Fe-ZSM-5 follows different reaction mechanisms over different iron sites.[71] Specifically, while CO is active over isolated iron species, the reduction of N_2O by hydrocarbons such as CH_4 and C_3H_8 happens more favorably over oligo-nuclear iron-oxo clusters.

Recently, *in situ* characterization and *operando* studies have provided insights into the active sites and reaction mechanism of the CH_4-SCR of N_2O over zeolite-based catalysts.[122–125] Campa *et al.* investigated N_2O reduction with CH_4 on metal-free H-NaMOR catalysts in the absence and presence of oxygen using *in situ* and *operando* FTIR methods.[122] It was suggested that N_2O and CH_4 are synergistically activated on dehydrated Si–OH–Al pairs as main active sites. In addition, formaldehyde-like species are possible reaction intermediates during the CH_4-SCR of N_2O. This observation is consistent with the other studies on Fe-MOR, Fe-FER, Co-MOR, and Ni-MOR catalysts that employed *in situ* UV-vis DRS and *operando* FTIR experiments.[123,125] The catalytic performance of Fe-MOR and Fe-FER catalysts were attributed to the stabilization of Fe^{II} species and bifunctional active sites, which consist of Fe^{III}-oxo species and nearby reactive OH species, in these zeolite frameworks.[123] In another study on CH_4-SCR of N_2O on Fe-BEA with *operando* IR and *in situ* XAFS-DRIFTS, Liu *et al.* found that both NO and NH_3 inhibit the reduction of N_2O due to their strong adsorption on Fe^{II} active sites and rapid reaction with Fe^{III}–OH and α-oxygen.[124]

In addition to Fe-zeolites, Rh/Al_2O_3, Ru/Al_2O_3, and Pd/Al_2O_3 have been studied for the HC-SCR of N_2O.[39,40] Christoforou *et al.* investigated Rh, Ru, Pd, Co, Cu, Fe, and In with various catalyst supports (Al_2O_3, SiO_2, TiO_2, ZrO_2, calcined hydrotalcite $MgAl_2(OH)_8 \cdot H_2O$) and found that Rh/Al_2O_3 and Ru/Al_2O_3 are the most active catalysts for HC-SCR of N_2O in the presence of excess O_2.[39] However, propene was found to facilitate N_2O reduction over Rh/Al_2O_3 by scavenging N_2O-derived O, helping maintain catalytically available Rh sites. Propene was found to potentially alter the redox state of active metal sites, lowering and inhibiting catalytic performance on Ru/Al_2O_3 as it reduces Ru^{3+}/Ru^{4+} sites that are active for N_2O decomposition. The presence of oxygen in the feed stream also hinders N_2O reduction over Rh/Al_2O_3 but alleviates the inhibition of propene over Ru/Al_2O_3, as O_2 oxidizes propene into CO and CO_2. Water was suggested to inhibit C_3H_6-SCR of N_2O in the presence of O_2 by competitive adsorption with N_2O and potentially the formation of Ru oxyhydroxides that alter electronic structure of active RuO_2 active sites. On the contrary, the presence of SO_2 impedes N_2O reduction by the formation of sulfate species, consistent with the findings of Konsolakis *et al.* for CH_4-SCR of N_2O over Pd/Al_2O_3.[40] It was noted that water effects were reversible, whereas SO_2 deactivation was irreversible.

3.3 Ammonia (NH_3-SCR)

Ammonia is another potential reductant for the SCR of N_2O over different catalysts such as metal-zeolites and metal oxides.[56,67,126–128] Mauvezin *et al.* evaluated the decomposition and reduction of N_2O by ammonia over several metals supported on FAU zeolite, including Rh, Ru, Pd, Co, Cu, Ni, and Fe.[75] It appeared that Fe-FAU was the most efficient catalyst for NH_3-SCR of N_2O in the presence of oxygen. In terms of reaction mechanism of NH_3-SCR of N_2O over Fe-zeolites, it was suggested that the addition of ammonia assists the decomposition of N_2O by removing the surface oxygen species (eqn (23) of eqn (20)–(23)).[64]

$$N_2O + * \rightarrow N_2 + O* \tag{20}$$

$$N_2O + O* \rightarrow N_2 + O_2 + * \tag{21}$$

$$2\ O* \rightarrow O_2 + 2* \tag{22}$$

$$3\ O* + 2\ NH_3 \rightarrow N_2 + 3\ H_2O + 3* \tag{23}$$

Zhang *et al.* proposed a more detailed reaction pathway and mechanism of NH_3-SCR of N_2O over Fe-MOR and Fe-BEA catalysts related to the redox cycle of Fe^{3+}–OH/Fe^{2+}–OH sites through $–NH_2$ and NO intermediates.[74] Multiple temperature programmed experimental techniques and FT-IR of N_2O/NH_3 interaction were employed. It was found that the rate-limiting step over Fe-MOR is reduction of Fe^{3+}–OH by ammonia into Fe^{2+}–OH and N≡N bond breaking was the main N_2O splitting mechanism. Similarly, N_2O oxidation of Fe^{2+}–OH was the rate-determining step for Fe-BEA with N–O bond breaking being the main N_2O splitting mechanism. The next reaction steps of nitric oxide in the presence of oxygen follow the typical SCR mechanism to form nitrogen and water (eqn (24)).

$$4\ NO + 4\ NH_3 + O_2 \rightarrow 4\ N_2 + 6\ H_2O \tag{24}$$

The high activity of Fe-MOR was ascribed to the pore structure of MOR zeolites and the high iron loading, which enable the genesis of proximal Fe^{3+} ions or $Fe^{3+}\cdots Fe^{3+}$ pairs as the active sites for the N≡NO splitting.

The zeolite structure strongly influences the distribution of iron species, which plays an important role in catalytic activity of Fe-zeolites for the N_2O decomposition and reduction by ammonia.[64] Wang *et al.* studied the nature of iron species by UV-vis, Mössbauer, and EPR spectroscopies, as well as H_2-TPR, and kinetic measurements.[24] It was found that isolated and binuclear Fe sites are present in Fe/SSZ-13, whereas Fe/BEA contains mostly oligomeric Fe_xO_y species and exhibited a higher NH_3-SCR activity compared to Fe/SSZ-13. This indicates that larger site ensembles, such as oligo-nuclear iron-oxo clusters, are the main active sites of the NH_3-SCR of N_2O instead of isolated iron species. A similar finding about the catalytic effect of zeolite structure on Fe-zeolites has been reported by Du *et al.*[109] The NH_3-SCR of N_2O activity followed the order: Fe-BEA > Fe-ZSM-5 > Fe-FAU > Fe-ZSM-35 > Fe-MCM-22 > Fe-SSZ-13. UV-vis DRS, XPS, and H_2-TPR analyses verified that Fe^{3+} sites are more favorably located inside straight-channel zeolite pores compared to cage-type zeolites, leading to the high activity observed in Fe-BEA and Fe-ZSM-5. In addition, Fe-zeolites with larger pore sizes facilitate the internal diffusion of N_2O inside zeolite channels, thereby improving the catalytic reduction of N_2O by ammonia. Zhang *et al.* performed H_2-TPR, UV-vis DRS, and NH_3/O_2-TPD to analyze the nature and distribution of iron species, including isolated Fe^{3+}, oligo-nuclear $Fe_x^{3+}O_y$ clusters, and Fe_2O_3 nanoparticles on external surface.[73] It was also determined that larger zeolite channels contain more exchanged Fe ions, which explains higher Fe loadings in Fe-MOR and Fe-USY compared to Fe-BEA and Fe-ZSM-5. Interestingly, it was suggested that isolated Fe^{3+} ions are active species for the reduction of N_2O, while the $Fe_x^{3+}O_y$ clusters are less active due to strong ammonia adsorption on Brønsted acid sites formed on the bridge oxide ions in binuclear iron species. On the other hand, *operando* electron paramagnetic resonance measurements were performed by Fischer *et al.* to elucidate the active sites and kinetically relevant reaction steps during N_2O decomposition and reduction over Fe-SSZ-13 with different reductants, including CH_4, NH_3, and H_2.[129] They found that isolated Fe^{2+} species in axial coordination are the main active sites for direct N_2O decomposition, while Fe_xO_y clusters and Fe^{2+} sites in distorted geometries are responsible for N_2O reduction in the presence of reductants.

Regarding the effect of other gases in the feed, it was reported that oxygen showed an inhibitory effect on NH_3-SCR of N_2O over Fe-MFI, Fe-FAU, Fe-BEA, and Fe-SSZ-13, likely due to the non-selective oxidation of ammonia.[24,75,127] However, the presence of oxygen had no significant influence on N_2O conversion over Fe-MOR whereas NH_3-SCR of N_2O outperformed ammonia oxidation.[73,74] While the influence of NO on N_2O reduction by NH_3 over Fe-MOR was negligible,[73] the reduction of N_2O by NH_3 over Fe-FER and Fe-BEA was promoted by NO, due to the fast surface reaction between adsorbed O* and NO* species.[64] On the contrary, Zhuang *et al.* found that a small fraction of NO (100 ppm) in the feed stream can inhibit the NH_3-SCR of N_2O over Pd/Al_2O_3 catalyst.[130] Interestingly, by modifying the Al_2O_3 support to create oxygen vacancies containing free electrons, the Pd-based catalyst exhibited superior performance in the low temperature regime below 300 °C, along with desirable NO inhibition resistance. Baek *et al.* studied the effect of water on the NH_3-SCR of N_2O over Fe-BEA using DRIFTS and self-consistent-charge density-functional-tight-binding calculations.[131] It was found that the presence of water vapor increases hydroxyl groups on the Fe-BEA surface. Instead of the conventional explanation, where the presence of water vapor leads to competitive adsorption, the authors attributed decreased N_2O conversion to surface hydroxyl groups that induce stronger adsorption of N_2O.

3.4 Hydrogen (H_2-SCR)

The research on N_2O reduction by hydrogen is limited (mainly reported with noble metal catalysts).[41,110] Hydrogen is not a selective reductant in the SCR of N_2O over Fe-BEA and RuO_2 catalysts, as it favorably reacts with oxygen present in the reactant feed.[56,67] Santiago *et al.* employed a combination of steady-state reaction tests at ambient pressure, transient reaction studies in the temporal analysis of products (TAP) reactor (see section 4.1), and DFT simulations to unravel the mechanism of decomposition and reduction of N_2O by hydrogen or ammonia on RuO_2.[56] It was found that hydrogen facilitates the reduction of the catalyst surface to form highly active oxygen vacancies, and it appears to be a more effective reductant compared to ammonia in this catalytic system, as ammonia-derived intermediates strongly adsorb on RuO_2 surface and block active sites for N_2O conversion. Arenas-Alatorre *et al.* studied N_2O decomposition and reduction by H_2 over Pt/SiO_2, Ni/SiO_2, and $NiPt/SiO_2$ catalysts, which showed much lower T_{50} values compared to other catalyst systems (Table 2).[41] It was found that the addition of H_2 improves N_2O conversion over studied monometallic and bimetallic catalysts. Bimetallic (6–8 nm NiPt) catalysts exhibited a higher activity compared to Pt/SiO_2 and Ni/SiO_2 catalysts in the H_2-SCR of N_2O, which was ascribed to the geometric and electronic effects of alloying. Another study of N_2O reduction by H_2 on noble metal substituted TiO_2 catalysts ($Ti_{0.99}M_{0.01}O_{2-\delta}$, where M = Ru, Rh, Pd, Pt) also reported significantly low T_{50} values (Table 2), notably for Pd-substituted TiO_2. The authors attributed the high activity to a bi-functional pathway: N_2O dissociation at oxide-ion vacancies and rapid H_2 activation on substituted metal ions that scavenge O* to produce H_2O; this mechanism was supported by H_2-TPR/uptake trends and kinetic modeling.[110] The reduction of N_2O by H_2 was also studied on various polyoxometalate-supported single-atom catalysts M_1/PTA (M = Fe, Co, Mn, Ru, Rh, Os, Ir, and Pt; PTA = $[PW_{12}O_{40}]^{3-}$) by DFT.[132] Os_1/PTA SAC exhibited high activity with a low rate-limiting energy barrier, which was attributed to a strong charge-transfer cooperative effect of metal and support along the favorable reaction pathways. The Os atom and PTA support acts as electron reservoirs, effectively modulating the adsorption/desorption and bond-breaking steps.

The comparison of different reductants for the SCR of N_2O is summarized in Table 3. The usage of CO and NH_3 can be cost-effective when available as a byproduct gas in industrial plants or when coupled with existing SCR systems.

Table 3 Comparison of different reductants for the SCR of N_2O

Reductants	Common catalysts	Estimated cost (catalyst, reductant)	By-products	Potential application
CO	Fe-zeolites	Low	CO_2	Power plant flue gas
CH_4	Fe-zeolites	Low	CO, CO_2, H_2O	Nitric acid production tail gas
NH_3	Fe-zeolites	Low	NO, N_2, H_2O	Ammonia-fueled engine exhaust
H_2	Noble metals	High	H_2O	Low-temperature constraints

Methane is a low-value hydrocarbon and the major component of the natural gas stream, enabling economical use in the SCR of N_2O. On the other hand, the industrial application of hydrogen is still limited due to the high costs associated with hydrogen production, transportation, and storage.

3.5 Catalyst durability and exotic reductants for SCR

The research on the catalyst durability in the selective catalytic reduction of N_2O remains limited. Zhang *et al.* reported that the catalytic activity of Fe-MOR for NH_3-SCR of N_2O remains almost unchanged for more than 100 hours under simulated nitric acid plant conditions at 427 °C with the presence of oxygen and water vapor in the feed stream.[133] It is worth noting that Fe-zeolites, which are the most common catalyst for the SCR of nitrous oxide, have also been studied extensively for the NH_3-SCR of nitric oxide, particularly in relation to treatment processes of exhaust gases from diesel engines, coal-fired plants, and industrial boilers.[134] The catalyst durability of Fe-zeolites in the NH_3-SCR of NO is significantly affected by sulfur and phosphorus poisoning, as well as their hydrothermal stability at elevated temperatures, which constrains their practical applications.[135]

In SCR reactors, other more exotic reductants may also play a key role in future N_2O abatement technologies. In addition to the CO, hydrocarbons, NH_3, and H_2 methods discussed previously, other reducing agents can be considered and new technologies envisioned. Expanding on carbonaceous reductants like CO and hydrocarbons, solid carbon species like coke, charcoal, and biochar could also be used. Wang *et al.* investigated the reduction of N_2O by biomass char with the presence of CO and O_2 in a fixed bed reactor system.[136] While biomass char and CO facilitated the reduction of N_2O by lowering both the onset temperature and the apparent activation energy, an inhibitory effect was observed with O_2. The solid carbon materials could also play a role as a catalytic surface as was observed by Xie *et al.*, who studied activated coke catalysts for SCR of NO.[137] Similarly, Wang *et al.* looked at the effect of cost effective and high surface area activated carbon at 200–300 °C in a 1000 ppm NO in N_2 gas stream.[138] They saw detection of CO and reduced NO after the reactor, indicating the carbon had reduced NO to N_2. As noted previously, the produced CO can further reduce other NO_x species. While neither group tested N_2O abatement, their results suggest a need for further study.

While ammonia is the most common reductant for SCR, other nitrogen species could also serve as reductants for N_2O. Urea is used in diesel exhaust fluid to mitigate NO_x, which thermally decomposes releasing ammonia for the standard NH_3-SCR mechanism.[139] While nitrogen in the −3 oxidation state (*e.g.* ammonia and urea) has the most electrons to contribute to N_2O reduction, nitrogen species in the −2 (*e.g.* hydrazine) and −1 oxidation states (*e.g.* hydroxylamine) could also be used. In one instance, Zheng *et al.* developed a kinetic model for NO removal by hydrazine, that could be similarly applied to N_2O.[140]

SO_x and NO_x are often emitted together from industrial processes but are typically removed individually using flue gas desulfurization followed by SCR.[141] Merging these processes has been explored through simultaneous catalytic desulfurization and denitrification (SCDD). Hydrogen sulfide has been used as a reductant in SCDD. Developing this technology, Lü *et al.* were able to achieve conversion rates of 75% for SO_2 and 90% for NO in the same reactor at 280 °C.[142] Separately, Yang *et al.* found that a sulfide-driven autotrophic denitrification step reduced N_2O emissions during a wastewater treatment system known as sulfate reduction-autotrophic denitrification–nitrification integrated process.[143] This process combined elements of the sulfur- and nitrogen-cycles, reducing nitrate ions in solution to nitrogen gas while oxidizing sulfide ions to sulfate/sulfite ions and elemental sulfur. The N_2O reduction rate scaled linearly with sulfide concentration at pH 7. While quite dissimilar to gas phase SCR, it highlights the principles of incorporating sulfide as a reductant for N_2O abatement.

4 Mechanistic investigation of nitrous oxide abatement

4.1 Temporal analysis of products (TAP) experiments

Fundamental understanding of reaction mechanisms and the nature of active sites are important to advance catalyst development for efficient chemical processing. Most of the experimental approaches on studying direct decomposition and SCR of N_2O are based on light-off curve measurements (*i.e.* tracking reactant conversion as a function of temperature). Transient kinetic studies of heterogeneous-catalyzed gas phase reactions in TAP reactors can be effectively utilized to obtain kinetic parameters (*e.g.*, rate constants of simple reaction steps, lifetime of reactive surface species, *etc.*) based on the time-dependent interactions between gas molecules and the catalyst surface, and offer deeper mechanistic insights into simple reaction steps

(Fig. 8A). A more detailed description of the TAP reactor and experiments were reported elsewhere.[144–147]

As mentioned in section 2 and 3, the reaction mechanism of direct decomposition and SCR of N_2O depend on the nature and distribution of active sites, leading to distinct catalyst performance. These correlations have been investigated on common N_2O abatement catalyst systems, including noble metals, metal oxides, and zeolites, in TAP reactors. Several studies have performed pulse response experiments to understand the mechanism and kinetics of N_2O abatement reactions with Fe-based catalysts.[71,147] Kondratenko and Pérez-Ramírez studied direct decomposition of N_2O in a TAP reactor and found that the direct decomposition of N_2O over steam-activated Fe-silicalite occurs on free, isolated iron species and iron sites associated with adsorbed mono-atomic oxygen species (*-O) at 500–575 °C.[149] They found that O_2 forms *via* decomposition of a bi-atomic oxygen species (*-O_2) adsorbed over the iron site. This species is derived from O-*-O, which is formed *via* interaction of N_2O with the iron site associated with (*-O). The recombination of *-O species or direct formation N_2O and *-O (Eley–Rideal) mechanisms were excluded. This N_2O decomposition pathway over Fe-silicalite was also applicable to Fe-ZSM-5, which has markedly different iron speciation including both isolated and oligomeric iron-oxo species, as well as small Fe_2O_3 nanoparticles, indicating the generality of the reaction mechanism.[150] In addition, the kinetic parameters of N_2O decomposition, such as turnover frequency of N_2 formation, rate constant and activation energy of elementary steps, were calculated from a TAP-derived kinetic model for the comparison between Fe-ZSM-5 and Fe-silicalite. The relative activities of these catalysts in the TAP experiment were found to be consistent with the steady-state performance. On the other hand, it was suggested that the oxygen is formed directly *via* the reaction of gas-phase N_2O with adsorbed mono-atomic oxygen species originating from the decomposition of adsorbed N_2O on Rh-ZSM-5 catalyst.[151] The higher catalytic activity of Rh-ZSM-5 compared to Fe-ZSM-5 was attributed to the stronger N_2O adsorption and faster oxygen formation to regenerate free active sites over rhodium sites.

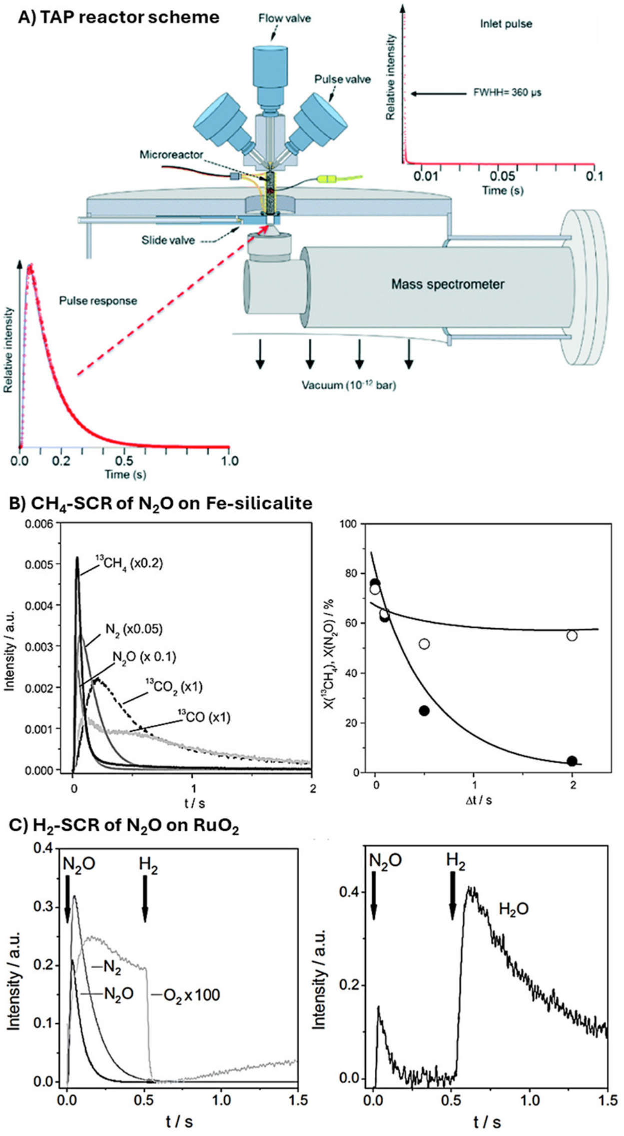

Fig. 8 (A) Schematic of a TAP reactor. Reprinted from ref. 147 under CC BY 3.0 license. (B) Transient responses of N_2O, $^{13}CH_4$, N_2, ^{13}CO, and $^{13}CO_2$ upon simultaneous pulsing of N_2O and $^{13}CH_4$ and conversion of $^{13}CH_4$ (●) and N_2O (○) as a function of the time delay (Δt) between the pulses of N_2O and $^{13}CH_4$ over Fe-silicalite at 450 °C (723 K). Reprinted from ref. 148 with permission from Elsevier. (C) Transient responses of N_2O, N_2, O_2, and H_2O in pump-probe experiments of $N_2O : Ar = 1:1$ and $H_2 : Xe = 1:1$ at 250 °C (523 K) with a time delay of 0.5 s between the pulsed mixtures. Reprinted from ref. 56 with permission from Elsevier.

The N_2O decomposition reaction mechanism at high temperature regime (550–700 °C) over $BaFeAl_{11}O_{19}$ hexaaluminate was investigated in the TAP reactor and compared with lower temperature regime (400–500 °C) over Fe-ZSM-5 zeolites.[56,152] Regardless of the catalyst support (hexaaluminate or ZSM-5), it was indicated that N_2O decomposition activity is more favorable over clustered iron species (Fe–O_x) than isolated iron sites. Large iron oxide particles were detrimental to activity, thus there is an optimum in clustering of iron species. Regardless of the catalyst support optimum in clustering. The NO-promoted N_2O decomposition over Fe-zeolites was investigated by multitrack experiments in a TAP-reactor-like high-vacuum reactor system.[153] The addition of nitric oxide benefits N_2O decomposition by removal of adsorbed oxygen atoms and facilitating migration and recombination of these atomic oxygen species on catalyst surface. Mechanistic studies of N_2O decomposition by transient kinetic methods were also performed over other materials such as Na-doped CaO, Pt gauze, and Pt–Rh gauze.[154–156] It is noted that the formation of gas-phase oxygen by recombination of two adsorbed oxygen atoms on surface Pt sites was less favorable under transient vacuum conditions as compared to ambient pressure steady-state conditions, which was ascribed to a low surface coverage of these atomic oxygen species in high-vacuum TAP reactor.[157] This observation further underscores the impact of surface coverage under relevant reaction conditions on the underlying mechanisms, which is of critical importance when extrapolating TAP-derived models to steady-state experiments. The reduction of N_2O over Fe-zeolites using CO, methane, and propane as reductants, was investigated by pump/probe pulse response experiments the TAP reactor (Fig. 8B).[56,148,156,158,159] Varying the time delay, Δt, between the N_2O and hydrocarbon pulse on Fe-silicalite shows that the reactive oxygen generated from N_2O on extra-framework Fe sites has a short lifetime, as evidenced by the decline in hydrocarbon conversion with increasing time delay.[156] The finding on the short lifetime of highly reactive oxygen species formed upon interaction of N_2O on extra-framework iron sites was consistent for both methane and propane, with the latter being a more effective reductant for N_2O reduction under both high vacuum TAP conditions and ambient pressure flow experiments.[148,159] Santiago *et al.* also used the pump/probe format pulsing N_2O followed by ammonia and hydrogen reductants over a RuO_2 catalyst. The time delay was fixed at 0.5 s, and as shown in Fig. 8C, the H_2 pulse suppresses the O_2 response from N_2O and increases yield of H_2O, indicating that N_2O-derived surface oxygen remains reactive over the 0.5 s window and is readily scavenged by H_2.[56] In addition, the promotion effect of H_2 and NH_3 on the N_2O reduction is diminished in the presence of oxygen due to non-selective oxidation reactions of these reductants.

4.2 Density functional theory (DFT) modeling

DFT enables atomic-level insight into catalytic mechanisms and electronic structure information, enabling it to be used both as an explanatory tool for the performance of a catalyst, and as a screening tool for catalyst discovery. The energy at each elementary reaction step, the activation energy between steps, and the energies of proposed catalytic intermediaries can be directly calculated. From these energetics, the active site(s), rate limiting step, and energetically favorable pathway can be determined. Additionally, DFT provides electronic structure information, notably the d-band center, Bader (partial) charge, charge density, and electronic density of states to rationalize catalytic performance. A more extensive treatment of DFT for catalysis and the background of methods can be found in literature.[160–162] It has been utilized for studies of supported metal, mixed oxide, and zeolite catalysts in both the direct decomposition and the SCR of N_2O.

Mechanistic studies with DFT for direct decomposition of N_2O have helped determine active sites, activation barriers, the role of promoters, and provided an electronic structure explanation. Kim *et al.* computationally studied the decomposition of N_2O on Pd_xCu_y compositions.[163] It was found that Pd adsorbs N_2O onto the metal surface stronger than Cu, while Cu more easily dissociates N_2O than Pd. Intermediate Pd_xCu_y compositions were found to have a balance of these traits leading to improved activity. The PdCu catalyst had only a slight reduction in N_2O adsorption strength *vs.* pure Pd (−38.58 *vs.* −42.45 kJ mol^{-1}), and a lower N_2O dissociation activation energy (8.70 *vs.* 24.14 kJ mol^{-1}). Electronic structure analysis found that the PdCu alloy had a higher d-band center position (−1.64 eV) *vs.* pure Pd (−1.67 eV) or Cu (−2.29 eV), which may enable higher catalytic activity. The Pd_3Cu alloy had the weakest O adsorption and highest predicted decomposition activity, which matches the experimental observations reported in literature.[32] Sun *et al.* conducted DFT calculations for alkaline-earth-modified metal oxide catalysts ($A_{0.5}Co_{2.5}O_4$ with A = Mg, Ca, Sr, Ba) in tandem with experiments for direct N_2O decomposition.[164] Ba was found to significantly lower the oxygen vacancy formation energy *vs.* the unmodified Co_3O_4 oxide (261.46 *vs.* 172.71 kJ mol^{-1}) for the near O site. The lower oxygen vacancy formation energy of $Ba_{0.5}Co_{2.5}O_4$ was attributed to the lower valency of Ba compared to Co. The oxygen vacancies in the oxide allowed the catalyst to chemisorb more O, which enables the reduction of N_2O, resulting in a 73 °C reduction in the T_{90} temperature for $Ba_{0.5}Co_{2.5}O_4$ *vs.* Co_3O_4. Wang *et al.* utilized DFT to investigate both the oxygen vacancy formation energy and the N_2O decomposition activation energy over oxygen vacancies and metal sites in CeO_2 and Co-doped CeO_2.[165] The doping of Co at a Co/Ce ratio of 1 was found to reduce the oxygen vacancy formation energy from 219.99 to −29.91 kJ mol^{-1}. Additionally, the activation energy over both the metal sites (224.81 *versus* 311.65 kJ mol^{-1}) and oxygen vacancies (111.92 *versus* 284.63 kJ mol^{-1}) were lower for the Co-doped CeO_2, indicating the oxygen vacancies serve as active sites for the direct decomposition of N_2O. Heyden *et al.* performed a comprehensive DFT study of the energetics and kinetics of direct N_2O decomposition on the hydrated and dehydrated mononuclear Fe sites in a Fe-ZSM-5 zeolite catalysts to determine the active sites, method of low concentration H_2O deactivation, and rate constants.[166] The decomposition was modeled following the E–R-like mechanism shown in eqn (25)–(29) (M = Fe mononuclear site, Z = zeolite site):

$$Z^-[M]^+ + N_2O \leftrightarrow Z^-[M]^+(ON_2) \tag{25}$$

$$Z^-[M]^+(ON_2) \leftrightarrow Z^-[MO]^+ + N_2 \tag{26}$$

$$Z^-[MO]^+ + N_2O \leftrightarrow Z^-[MO]^+(ON_2) \tag{27}$$

$$Z^-[MO]^+(ON_2) \leftrightarrow Z^-[M]^+(O_2) + N_2 \tag{28}$$

$$Z^-[M]^+(O_2) \leftrightarrow Z^-[M]^+ + O_2 \tag{29}$$

The $Z^-[Fe]^+$ and $Z^-[FeO]^+$ had exothermic enthalpies of adsorption for N_2O; however, the oxidation of bare $Z^-[Fe]^+$ by N_2O is very exothermic (−259.5 kJ mol^{-1} or −2.69 eV), making the reverse reaction unlikely to occur during N_2O decomposition, making $Z^-[FeO]^+$ the active site. After determining $Z^-[FeO]^+$ was the active site, H_2O adsorption and potential catalyst deactivation were evaluated. H_2O absorbs without barriers to $Z^-[FeO]^+$, forming $Z^-[Fe(OH)_2]^+$, which has a higher activation energy for N_2O decomposition. The formation of $Z^-[Fe(OH)_2]^+$ sites resulted in a more than doubling of the activation energy from (106.7–229.3 kJ mol^{-1}) as water content increased from 0 to 100 ppb.

SCR of N_2O with a variety of reductant agents has also been studied using DFT.[111,167] The reaction pathways on isolated iron sites and Fe_2O_3 particles on a Fe/ZSM-5 catalyst for CO-SCR previously discussed in section 3.1 and superior performance of the CO-SCR *versus* direct decomposition were supported by DFT calculations.[111] DFT simulations showed the pristine Fe_2O_3 is unable to adsorb N_2O initially and required an oxygen vacancy for N_2O adsorption to occur. With the oxygen vacancy being formed by CO oxidation the CO-SCR follows the MvK mechanism. On the isolate iron sites CO was unable to adsorb, causing initial N_2O adsorption and release of N_2, followed by CO bonding with O* forming CO_2 for subsequent desorption, thus following the E–R reaction mechanism. For both the isolated Fe site and the on Fe_2O_3 the desorption of CO_2, a product of CO-SCR, had a far lower activation energy than that of O_2, a product of direct N_2O decomposition, explaining the improved low temperature regime (300–250 °C) conversion efficiency of CO-SCR. When NO is used as a reductant, it can activate the catalytically inactive $Z^-[Fe(OH)_2]^+$ sites, by absorbing and subsequently forming HNO_2, which is easily desorbed leaving catalytically active $Z^-[FeOH]^+$ sites, resulting in improved decomposition performance below 427 °C (700 K).[167] Further studies involving more complex alloy compositions may be a critical step in developing next generation catalysts.

5 Outlook

5.1 High-throughput experimentation and machine learning for catalyst discovery

High-throughput (HT) synthesis and screening coupled with computationally guided design are essential as the exploratory compositional space continues to grow for novel catalytic discovery. Limited throughput of single-channel reactors hinders the ability to achieve rapid materials discovery.[168] HT reactor testing is beneficial for rapid materials discovery due to the ability to test multiple catalysts simultaneously, which greatly decreases the time needed to test a large number of catalysts within a compositional design space.[169–171] In general, HT experimentation has been implemented to test up to 48 different catalysts at a single time.[172–174] The ability to collect large amounts of data from HT experimentation allows for the development of machine learning (ML) models to probe the complex design space and determine which features are important for specific reactions.[175]

Currently, only a limited number of studies utilize HT experimentation to develop N_2O abatement catalysts. In one study, Li *et al.* utilized HT experimentation to analyze a variety of N_2O decomposition catalysts under the same reaction conditions. A reactor capable of testing 48 catalysts simultaneously was used. The activity across many catalysts was related back to the characteristics of the catalyst, such as the impact of the support and pretreatment conditions.[21] Another study by Hendershot *et al.* investigated the optimization of a NO_x storage and reduction catalyst by using a statistical design of experiments model coupled with HT experimentation.[176] The HT setup quantified the production of N_2O from the catalysts as one of the factors analyzed. This work demonstrates the ability to analyze N_2O in an HT setup, which highlights the potential for further applications in future N_2O abatement technologies.

Recent studies have also applied ML to predict the N_2O emissions from wastewater treatment and agricultural crop production, two of the largest sources to global N_2O emissions (see Fig. 1).[177,178] Additionally, ML has been employed to predict the adsorption of N_2O on activated carbon and carbon molecular sieves.[179] A major development in computational studies that can be leveraged for catalytic N_2O abatement is machine-learned interatomic potentials (MLIPs). MLIPs, such as M3GNet, are trained on large databases of DFT data with neural networks to learn the underlying features to property relationships and use this to form universal interatomic potentials.[180] MLIPs provide DFT level accuracy for the energetics of elementary reaction steps at a fraction of the computational cost (~4–7 orders of magnitude faster). Furthermore, MLIPs enable the inclusion of time and temperature effects to capture the modelling of realistic catalyst dynamics.[181] Coupled, these provide a very powerful tool for catalyst discover. However, to date, MLIPs have not been utilized in the literature for catalytic N_2O abatement and have only been used to study ternary oxides for syngas conversion and a NO + CO reaction.[182,183] Leveraging MLIPs for N_2O abatement studies would enable both more accurate activity predictions by incorporating the catalyst evolution and would also facilitate the exploration of exponentially larger compositional space of the catalysts.

Coupling experimentation and computational data with ML model development can allow researchers to take advantage of active learning (AL) to predict optimal catalysts while using HT experimentation to test large amounts of data. This approach has been utilized for NH_3 synthesis catalysts. A feature space of descriptors to characterize a promoted Ru catalyst for NH_3 synthesis was subdivided into reaction conditions, metal–support interactions, promoter–support interactions, metal–promoter interactions, catalyst preparation, and catalyst pretreatment, for a total of 536 features, which was reduced to 160 after feature selection. For AL to find the best performing promoters, the feature space was reduced again from 160 to 53 to limit it to only features that vary with the promoter. The AL predicted top performing promoter was synthesized and tested with HT experimentation, and the data added for the subsequent prediction.[170] Another ML approach was developed by Wang *et al.* that divided the feature space into catalyst composition, preparation conditions, and reaction conditions for the NH_3

for NO_x. The advantage of this feature space is it allows the catalyst composition to be optimized.[184] Though not explicitly studying N_2O abatement catalysts, these previous studies highlight the features and methodologies that have been proven effective and can be applied to these reactions.

Future studies coupling high-throughput experimentation with machine learning are imperative for catalytic discovery and optimization of novel catalysts for N_2O abatement reactions. This methodology will allow for rapid material screening to facilitate novel catalytic discovery at a more rapid pace while elucidating trends with ML.

5.2 Industrial outlook for catalytic design

In many industrial plants, such as nitric acid and adipic acid, N_2O is not a "pure" byproduct but is rather produced in an effluent with other gases that may be inhibiting. With this comes an opportunity to develop novel catalysts that are tailored towards being resistant to other inhibiting gases. Many industrial pollutants, such as water and SO_2, are emitted in addition to N_2O. As previously discussed in section 2.4 and 3.5, these other additional gases in the feed stream inhibit catalytic activity and can result in irreversible deactivation of the catalyst. These considerations motivate the need for the discovery of resilient catalysts through the altering of the support or the addition of promoters to influence the binding of reactants and inhibitors. Many studies have begun to analyze catalyst compositions to improve their toxicity resistance. In short, other research groups have found that the addition of CeO_2 to a catalyst can increase water resistance with the synthesis of the catalysts also having an impact on the performance in the presence of catalytic toxins.[13,21,35] In addition, a different review article summarized that the toxicity resistance can be further improved upon through the synthesis of varied structure materials, such as core–shell type catalysts or through doping the catalyst with other elements, such as Ti, Zn, or K as these dopants can further weaken the binding of these catalytic toxins to the active sites.[13,185–187] Though there have been studies first analyzing how to improve the toxicity resistance of abatement catalysts, there is still a drive to further develop catalysts that can be resistant to industrial pollutants while achieving high activity, increased longevity, and decreased cost. In addition, with the development of novel catalysts, it is imperative to assess the longevity of the catalysts in realistic industrial conditions as increasing the catalysts lifetime will help save industrial operating costs. Other considerations for novel catalyst design should include catalyst cost, increasing activity at lower temperatures, as well as minimizing the environmental footprint for the large-scale synthesis and utilization of these catalysts. High performing catalysts, as seen with the direct decomposition section, include noble metals with the incorporation of other elements as promoters or supports, such as rare earth metals. This combination of materials may be active, but it may also come with tradeoffs in terms of cost deeming large-scale implementation challenging. Through larger studies, novel active materials and combinations of metals, supports, and promoters can be found while reducing expensive component weight loadings to decrease costs. With these additional considerations in mind, ML and HT experiments can be utilized to more rapidly achieve industrial N_2O abatement goals.

In conjunction with the opportunities for catalytic design for these industrial applications, there also comes additional challenges with the integration of these systems into large-scale industrial units. One challenge that will be faced involves the reactor design to allow for effective conversion of N_2O. This can be done by designing packed bed reactors with monoliths or with the use of membrane reactors to further enhance catalytic activity. In addition, new reactor designs come with the consideration of pressure drop through the catalytic bed. With a pressure drop in the system, it will become more costly for operations not only in energy requirements but because it can alter the thermodynamics of the reaction and negatively impact catalytic activity. This problem can be further mitigated by developing pelletized catalysts or through the synthesis of monoliths. In addition, there is further work needed to be done to assess how these catalysts perform in conjunction with other catalytic systems, such as de-NO_x, to ensure selectivity and decomposition of all harmful products. As these new industrial reactor designs are studied, chosen catalytic systems should be subjected to longevity tests to ensure sufficient catalytic activity in the industrial gas streams.

Following catalytic design considerations, further work is also needed in the work of technoeconomic analysis and life cycle analysis. A technoeconomic analysis would be able to help researchers and industry determine if an effective catalytic design is economically viable for large-scale applications. As mentioned, some catalysts may show higher activity but are hindered for further usage due to high cost of materials. However, there may be tradeoffs with choosing cheaper materials that may not have as high of activity but will meet N_2O abatement requirements. In addition, lifecycle analysis should be performed to analyze the environmental impact of the catalysts used from their creation to their disposal. This can aid in helping companies choose materials for their catalytic reactor systems that are less environmentally harmful to better align with industrial goals of reducing their carbon footprint.

6 Conclusions

Various catalytic designs for N_2O abatement were reviewed, with a specific focus on direct decomposition and selective catalytic reduction (SCR) pathways. Mechanistic insights for different catalytic systems, supported by transient kinetic studies and density functional theory calculations were also discussed. The review emphasizes viable operating conditions and mechanisms, highlighting three main catalyst-based designs of supported metal, metal oxide, and zeolite catalysts.

Previous studies have identified Rh as one of the most active metals for direct decomposition, with the choice of support playing a crucial in regenerating catalytic active sites. Metal oxide catalysts, such as Co_3O_4, Mn_2O_3, CuO, and NiO, as well as Fe-, Co-, and Cu-exchanged zeolites, have also emerged as promising, cost-effective alternatives to noble metal-based catalysts. Additionally, the incorporation of alkali metals and lanthanides as promoters has been shown to increase the catalytic activity by improving redox properties and promoting oxygen desorption from catalyst surfaces, thereby offering an opportunity to further lower respective T_{50} values.

The addition of reductants for SCR shifts the N_2O conversion towards lower T_{50} values, as shown across various catalyst systems (*e.g.*, Fe-zeolites, Rh-FAU, RuO_2, and metal oxides). Reductants (*i.e.*, CO, hydrocarbons, NH_3, and H_2) effectively aid in N_2O abatement by promoting the removal of the adsorbed oxygen species and reducing the temperature required for N_2O conversion. H_2 achieves the lowest T_{50} median temperature (129 °C) for the SCR catalysts, whereas hydrocarbons exhibited the highest at temperature (413 °C for C_3H_6). However, it should be noted that comparing the efficiency of reductants is not trivial, as the performance depends on the catalyst active sites-reductant interaction, as well as reaction conditions.

Fe-zeolites (*e.g.*, Fe-MFI, Fe-MOR, Fe-BEA, and Fe-SSZ-13) are extensively studied for their high N_2O-SCR activity, low cost, and low toxicity, which makes them suitable for industrial applications. Moreover, the SCR catalysts reported a lower median T_{50} (374 °C) than direct decomposition (432 °C). Among the catalyst classes (supported metals, metal oxides, and zeolites), the metal oxide catalysts achieved the lowest T_{50} values (350 °C and 216 °C for direct decomposition and SCR, respectively).

Future catalytic design must be tailored to be robust against common impurity gases found in industrial sources, such as O_2, H_2O, NO, and SO_2. The literature suggests that O_2 desorption is a rate-limiting step in the direct decomposition of N_2O and also inhibits the SCR of N_2O. Overall, the presence of O_2 and H_2O typically hinders both abatement processes through competitive adsorption, non-selective oxidation of reductants, and alteration of the surface redox state of the catalyst. Coupling machine learning (ML) with high throughput (HT) experiments offers a promising approach to rapidly screen catalytic materials and gaseous reaction feeds for enhanced catalytic activity while tailoring different considerations towards industrial concerns and applications.

Author contributions

Conceptualization: DDR. Data curation: HC, SS. Funding acquisition: DDR, MC. Investigation: HC, SS, MNG, MM. Project administration: DDR, JL, RF, DA, MC. Supervision: DDR, JL, RF, DA, MC. Visualization: HC, SS, MNG, MM. Writing – original draft: HC, SS, MNG, MM. Writing – review & editing: HC, SS, MNG, MM, DDR.

Conflicts of interest

There are no conflicts to declare.

Data availability

No primary research results, software or code have been included, and no new data were generated or analysed as part of this review.

Acknowledgements

The authors acknowledge the following funding sources: Battelle Savannah River Alliance, LLC under Contract No. 89303321CEM000080 with the U.S. Department of Energy. Publisher acknowledges the U.S. Government license to provide public access under DOE Public Access Plan (http://energy.gov/downloads/doe-public-access-plan) (MNG, MC, DDR). Battelle Energy Alliance, LLC under contract DE-AC07-05ID14517 with the U.S. Department of Energy (HC, RF). LAB 23-EM001 Hanford Tank Waste Cleanup R&D Program, U.S. Department of Energy, Environmental Management Office, Laboratory Policy Office (DDR). Laboratory Directed Research and Development (LDRD) Program within the Savannah River National Laboratory (MNG, MC).

References

1 O. D. Frutos, G. Quijano, A. Aizpuru and R. Munoz, *Biotechnol. Adv.*, 2018, **36**, 1025–1037.
2 United Nations Environment Programme (UNEP), Drawing Down N_2O to Protect Climate and the Ozone Layer. A UNEP Synthesis Report, Nairobi, Kenya, 2013.
3 J. Pérez-Ramírez, F. Kapteijn, K. Schöffel and J. A. Moulijn, *Appl. Catal., B*, 2003, **44**, 117–151.
4 X. Lan, K. W. Thoning and E. J. Dlugokencky, Trends in globally-averaged CH_4, N_2O, and SF_6 determined from NOAA Global Monitoring Laboratory measurements (Version 2025-05), Repository, 2025, DOI: 10.15138/P8XG-AA10.
5 G. Zhu, H. Shi, L. Zhong, G. He, B. Wang, J. Shan, P. Han, T. Liu, S. Wang, C. Liu, N. Zhang, L. Jiang, L. Yu, C. Zhan, Z. Tang, T. Wen, B. Ma, X. Su, S. Zhang, J. Zhang, H. Di, L. Hou, A. H. Krichels, M. Trimmer, M. S. M. Jetten, Y. Peng, F. E. Löffler, H. Tian and Y.-G. Zhu, *Nat. Rev. Earth Environ.*, 2025, **6**, 574–592.
6 W. Jörß, S. Ludig and L. Schneider, *Mitigation potentials for emissions of nitrous oxide from chemical industry in industrialised countries world-wide*, Öko-Institut e.V., Freiburg, Germany, 2023.
7 A. Shimizu, K. Tanaka and M. Fujimori, *Chemosphere*, 2000, **2**, 425–434.
8 K. Rafiq, M. Sabir, I. Sadia, M. Z. Abid, M. A. Nadeem and E. Hussain, *Mater. Adv.*, 2025, **6**, 8239–8276.

9 M. Qian, B. Guan, Z. Zhuang, J. Chen, L. Zhu, Z. Ma, X. Hu, C. Zhu, S. Zhao, K. Shu, H. Dang, T. Zhu and Z. Huang, *Catal. Sci. Technol.*, 2025, **15**, 2061–2103.

10 Y. Zhang, Z. Tian, L. Huang, H. Fan, Q. Hou, P. Cui and W. Wang, *Catalysts*, 2023, **13**, 943.

11 M. Konsolakis, *ACS Catal.*, 2015, **5**, 6397–6421.

12 X. Wu, J. Du, Y. Gao, H. Wang, C. Zhang, R. Zhang, H. He, G. Lu and Z. Wu, *Chem. Soc. Rev.*, 2024, **53**, 8379–8423.

13 Z. Zhuang, B. Guan, J. Chen, C. Zheng, J. Zhou, T. Su, Y. Chen, C. Zhu, X. Hu, S. Zhao, J. Guo, H. Dang, Y. Zhang, Y. Yuan, C. Yi, C. Xu, B. Xu, W. Zeng, Y. Li, K. Shi, Y. He, Z. Wei and Z. Huang, *Chem. Eng. J.*, 2024, **486**, 150374.

14 L. Xu, B. Guan, L. Zhu, S. Chang, J. Ma, R. Wang, D. Yang, T. Zhu, H. Qu, B. Tan and Z. Huang, *J. Environ. Chem. Eng.*, 2026, **14**, 122211.

15 Y. Bai, B. Guan, L. Zhu, S. Chang, J. Ma, R. Wang, D. Yang, T. Zhu, K. Shu, Z. Zhuang, X. Hu, C. Zhu, S. Zhao, J. Chen, J. Gao, H. Dang, L. Zhang, Y. Li, L. Xu, W. Zeng, S. Chen, L. Wang, C. Zhu, J. He, Q. Xian and Z. Huang, *Energy*, 2026, **351**, 140790.

16 J. Gao, B. Guan, L. Zhu, S. Chang, J. Ma, R. Wang, D. Yang, T. Zhu, H. Qu, B. Tan and Z. Huang, *Fuel*, 2026, **419**, 138780.

17 A. Bhan and W. N. Delgass, *J. Catal.*, 2022, **405**, 419–429.

18 M. Boudart, *Chem. Rev.*, 1995, **95**, 661–666.

19 E. A. Davidson and D. Kanter, *Environ. Res. Lett.*, 2014, **9**, 105012.

20 Y. Wu, Y. Zheng and P. Granger, in *Advances in Catalysts Research*, ed. S. J. Ikhmayies, Springer Nature Switzerland, Cham, 2024, pp. 221–257, DOI: 10.1007/978-3-031-49108-5_7.

21 Y. Li, A. Sundermann, O. Gerlach, K.-B. Low, C. C. Zhang, X. Zheng, H. Zhu and S. Axnanda, *Catal. Today*, 2020, **355**, 608–619.

22 N. Zhang, C. He, Y. Jing, Y. Qian, Y. Qin, H. Lin, M. Obuchi, R. Toyoshima, H. Kondoh and K. Oka, *Angew. Chem.*, 2025, **137**, e202517403.

23 K. S. Egorova and V. P. Ananikov, *Angew. Chem., Int. Ed.*, 2016, **55**, 12150–12162.

24 A. Wang, Y. Wang, E. D. Walter, R. K. Kukkadapu, Y. Guo, G. Lu, R. S. Weber, Y. Wang, C. H. F. Peden and F. Gao, *J. Catal.*, 2018, **358**, 199–210.

25 P. Boroń, L. Chmielarz, J. Gurgul, K. Łątka, B. Gil, B. Marszałek and S. Dzwigaj, *Microporous Mesoporous Mater.*, 2015, **203**, 73–85.

26 M. Rutkowska, L. Chmielarz, D. Macina, Z. Piwowarska, B. Dudek, A. Adamski, S. Witkowski, Z. Sojka, L. Obalová, C. J. Van Oers and P. Cool, *Appl. Catal., B*, 2014, **146**, 112–122.

27 S. Parres-Esclapez, L. Such-Basanez, M. J. Illan-Gomez, C. Salinas-Martinez de Lecea and A. Bueno-Lopez, *J. Catal.*, 2010, **276**, 390–401.

28 F. Lin, T. Andana, Y. Wu, J. Szanyi, Y. Wang and F. Gao, *J. Catal.*, 2021, **401**, 70–80.

29 V. A. Kondratenko and M. Baerns, *J. Catal.*, 2004, **225**, 37–44.

30 Y. Sun, Y. Wu, H. Wang and Z. Wu, *Environ. Sci. Technol.*, 2025, **59**, 24777–24785.

31 E. Wilczkowska, K. Krawczyk, J. Petryk, J. Sobczak and Z. Kaszkur, *Appl. Catal., A*, 2010, **389**, 165–172.

32 G. Pekridis, C. Athanasiou, M. Konsolakis, I. V. Yentekakis and G. E. Marnellos, *Top. Catal.*, 2009, **52**, 1880–1887.

33 E. Pachatouridou, E. Papista, E. F. Iliopoulou, A. Delimitis, G. Goula, I. V. Yentekakis, G. E. Marnellos and M. Konsolakis, *J. Environ. Chem. Eng.*, 2015, **3**, 815–821.

34 J. P. Dacquin, C. Dujardin and P. Granger, *Catal. Today*, 2008, **137**, 390–396.

35 H. Zhu, Y. Li and X. Zheng, *Appl. Catal., A*, 2019, **571**, 89–95.

36 J. Haber, M. Nattich and T. Machej, *Appl. Catal., B*, 2008, **77**, 278–283.

37 N. Zhang, C. He, Y. Jing, Y. Qian, T. Toyao and K.-i. Shimizu, *Surf. Interfaces*, 2024, **46**, 104120.

38 M. Konsolakis, C. Drosou and I. V. Yentekakis, *Appl. Catal., B*, 2012, **123–124**, 405–413.

39 S. C. Christoforou, E. A. Efthimiadis and I. A. Vasalos, *Catal. Lett.*, 2002, **79**, 137–147.

40 M. Konsolakis, I. V. Yentekakis, G. Pekridis, N. Kaklidis, A. C. Psarras and G. E. Marnellos, *Appl. Catal., B*, 2013, **138–139**, 191–198.

41 J. Arenas-Alatorre, A. Gómez-Cortés, M. Avalos-Borja and G. Díaz, *J. Phys. Chem. B*, 2005, **109**, 2371–2376.

42 T. Yamashita and A. Vannice, *J. Catal.*, 1996, **161**, 254–262.

43 M. Zabilskiy, P. Djinovic, E. Tchernychova and A. Pintar, *Appl. Catal., B*, 2016, **197**, 146–158.

44 L. Xue, H. He, C. Liu, C. Zhang and B. Zhang, *Environ. Sci. Technol.*, 2008, **43**, 890–895.

45 F. Zhao, D. Wang, X. Li, Y. Yin, C. Wang, L. Qiu, J. Yu and H. Chang, *Ind. Eng. Chem. Res.*, 2022, **61**, 13854–13862.

46 B. M. Abu-Zied, S. A. Soliman and A. Asiri, *Appl. Surf. Sci.*, 2019, **479**, 148–157.

47 H. Liu, J. Chen, Y. Wang, S. Xiong, Z. Su, Y. Wang, W. Yang, X. Chu, W. Yang, Y. Peng, W. Si and J. Li, *Chem. Eng. J.*, 2021, **414**, 128643.

48 Z. Zhang, Y. Wu, Y. Sun, H. Wang, Z. Wu and X. Wu, *ACS ES&T Eng.*, 2024, **4**, 2542–2552.

49 Y. Sun, Y. Wu, Z. Zhang, X. Wu, H. Wang and Z. Wu, *ChemCatChem*, 2025, **17**, e202401060.

50 H. Yu, Y. Li, Y. Du, Y. Pan, L. Yang, R. Han, W. Shan and Y. Xiong, *Sep. Purif. Technol.*, 2026, **382**, 136112.

51 H. Yu, Y. Li, Y. Pan, Y. Du, X. Feng, J. Cui, Z. Lou, W. Shan and Y. Xiong, *Chem. Eng. J.*, 2025, **504**, 159032.

52 K. Wang, Y. Du, Y. Li, X. Qi, W. Shan, H. Yu and Y. Xiong, *Mol. Catal.*, 2024, **569**, 114604.

53 R. Wu, Q. Wang, R. Wang, X. Lin, H. Dang, L. Li, S. Hu, M. Yang, K. Zheng, L. Zhang, Y. Wang and Y. Zhao, *ChemCatChem*, 2025, **17**, e202401659.

54 X. Hu, J. Meng, L. Feng, Y. Gao, Y. Wang and Y. Zhao, *Catal. Lett.*, 2024, **154**, 4367–4377.

55 Q. Wang, W. Yang, H. Dang, L. Li, R. Wu, Y. Wang and Y. Zhao, *J. Environ. Chem. Eng.*, 2024, **12**, 112463.

56 M. Santiago, V. A. Kondratenko, E. V. Kondratenko, N. López and J. Pérez-Ramírez, *Appl. Catal., B*, 2011, **110**, 33–39.

57 B. Li, X. Duan, T. Zhao, B. Niu, G. Li, Z. Zhao, Z. Yang, D. Liu, F. Zhang, J. Cheng and Z. Hao, *Environ. Sci. Technol.*, 2024, **58**, 2153–2161.

58 T. Ishihara, M. Ando, K. Sada, K. Takiishi, K. Yamada, H. Nishiguchi and Y. Takita, *J. Catal.*, 2003, **220**, 104–114.

59 K. S. Chang, H.-J. Lee, Y.-S. Park and J.-W. Woo, *Appl. Catal., A*, 2006, **309**, 129–138.

60 K. Pacultová, L. Obalová, F. Kovanda and K. Jirátová, *Catal. Today*, 2008, **137**, 385–389.

61 K. S. Chang and X. Peng, *J. Ind. Eng. Chem.*, 2010, **16**, 455–460.

62 X. Zhang, Q. Shen, C. He, C. Ma, J. Cheng, Z. Liu and Z. Hao, *Catal. Sci. Technol.*, 2012, **2**, 1249–1258.

63 Z. Sobalik, K. Jíša, D. Kaucký, A. Vondrová, Z. Tvarůžková and J. Nováková, *Catal. Lett.*, 2007, **113**, 124–129.

64 A. Guzmán-Vargas, G. Delahay and B. Coq, *Appl. Catal., B*, 2003, **42**, 369–379.

65 J. B. Lim, S. H. Cha and S. B. Hong, *Appl. Catal., B*, 2019, **243**, 750–759.

66 M. Wu, X. Chen, L. Zhong, H. Wang, X. Zhang, Q. Shen, W. Wei and Y. Sun, *Greenhouse Gases: Sci. Technol.*, 2016, **6**, 710–723.

67 G. Delahay, M. Mauvezin, A. Guzmán-Vargas and B. Coq, *Catal. Commun.*, 2002, **3**, 385–389.

68 J. Pérez-Ramírez, F. Kapteijn and A. Brückner, *J. Catal.*, 2003, **218**, 234–238.

69 J. Pérez-Ramírez, M. S. Kumar and A. Brückner, *J. Catal.*, 2004, **223**, 13–27.

70 M. D. Boutarbouch, J. G. Cortés, M. S. El Begrani, C. S. M. de Lecea and J. Perez-Ramirez, *Appl. Catal., B*, 2004, **54**, 115–123.

71 M. N. Debbagh, C. S. M. d. Lecea and J. Pérez-Ramírez, *Appl. Catal., B*, 2007, **70**, 335–341.

72 Q. Shen, L. Li, C. He, H. Tian, Z. Hao and Z. P. Xu, *Appl. Catal., B*, 2009, **91**, 262–268.

73 X. Zhang, Q. Shen, C. He, C. Ma, J. Cheng and Z. Hao, *Catal. Commun.*, 2012, **18**, 151–155.

74 X. Zhang, Q. Shen, C. He, C. Ma, J. Cheng, L. Li and Z. Hao, *ACS Catal.*, 2012, **2**, 512–520.

75 M. Mauvezin, G. Delahay, B. Coq and S. Kieger, *Appl. Catal., B*, 1999, **23**, L79–L82.

76 H. Yoshida, T. Tsuruta, Y. Yazawa and T. Hattori, *Appl. Catal., A*, 2007, **325**, 50–56.

77 A. Wang, J. Li and T. Zhang, *Nat. Rev. Chem.*, 2018, **2**, 65–81.

78 K. Liu, Y. Tang, Z. Yu, B. Ge, G. Ren, Y. Ren, Y. Su, J. Zhang, X. Sun, Z. Chen, X. Liu, B. Qiao, W.-Z. Li, A. Wang and J. Li, *Sci. China Mater.*, 2020, **63**, 949–958.

79 S. Bao, X. Lu, L. Yu, Y. Song, H. Fu, X. Qu, J. Y. Park and S. Zheng, *Appl. Catal., A*, 2025, **693**, 120122.

80 Q. Wang and D. Astruc, *Chem. Rev.*, 2019, **120**, 1438–1511.

81 F. Abbasi and C. Ghotbi, *J. Environ. Chem. Eng.*, 2025, **13**, 118757.

82 H. Tang, Y. He, P. Liu, J. Shao, F. Lin and Z. Wang, *Energy Fuels*, 2021, **35**, 18664–18679.

83 P. Zhao, F. Qin, Z. Huang, C. Sun, W. Shen and H. Xu, *Chem. Eng. J.*, 2018, **349**, 72–81.

84 Y. Jing, K. Taketoshi, N. Zhang, C. He, T. Toyao, Z. Maeno, T. Ohori, N. Ishikawa and K.-i. Shimizu, *ACS Catal.*, 2022, **12**, 6325–6333.

85 Y. Jing, C. He, N. Zhang, Y. Murano, R. Toyoshima, H. Kondoh, Y. Kageyama, H. Inomata, T. Toyao and K.-i. Shimizu, *ACS Catal.*, 2023, **13**, 12983–12993.

86 Structure Commission of the International Zeolite Association, *Atlas of Zeolite Framework Types*, Elsevier Science B.V., 2007.

87 L. S. Dent and J. V. Smith, *Nature*, 1958, **181**, 1794–1796.

88 G. T. Kokotailo, S. L. Lawton, D. H. Olson and W. M. Meier, *Nature*, 1978, **272**, 437–438.

89 P. Simoncic and T. Armbruster, *Am. Mineral.*, 2004, **89**, 421–431.

90 J. B. Higgins, R. B. LaPierre, J. L. Schlenker, A. C. Rohrman, J. D. Wood, G. T. Kerr and W. J. Rohrbaugh, *Zeolites*, 1988, **8**, 446–452.

91 P. T. Fanson, M. W. Stradt, J. L. Lauterbach and W. N. Delgass, *Appl. Catal., B*, 2002, **38**, 331–347.

92 D. C. Cano-Blanco, J. W. A. Fischer, F. Buttignol, I. Alxneit, G. Jeschke, O. Kröcher and D. Ferri, *ACS Catal.*, 2025, **15**, 15579–15595.

93 G. E. Marnellos, E. A. Efthimiadis and I. A. Vasalos, *Appl. Catal., B*, 2003, **46**, 523–539.

94 L. Xue, C. Zhang, H. He and Y. Teraoka, *Appl. Catal., B*, 2007, **75**, 167–174.

95 M. Konsolakis, I. V. Yentekakis, G. Pekridis, N. Kaklidis, A. C. Psarras and G. E. Marnellos, *Appl. Catal., B*, 2013, **138–139**, 191–198.

96 A. Serrano-Lotina, S. Pérez-Ferreras, C. Álvarez-Galván, R. E. Rojas-Hernandez, J. F. Fernández, P. Ávila, M. A. Bañares and F. Rubio-Marcos, *Chem. Eng. J.*, 2025, **524**, 169338.

97 S. N. Basahel, M. Mokhtar, T. T. Ali and K. Narasimharao, *Catal. Today*, 2020, **348**, 166–176.

98 G. Sádovská, E. Tabor, P. Sazama, M. Lhotka, M. Bernauer and Z. Sobalík, *Catal. Commun.*, 2017, **89**, 133–137.

99 F. Buttignol, D. Rentsch, I. Alxneit, A. Garbujo, P. Biasi, O. Kröcher and D. Ferri, *Catal. Sci. Technol.*, 2022, **12**, 7308–7321.

100 I. Melián-Cabrera, C. Mentruit, J. A. Z. Pieterse, R. W. van den Brink, G. Mul, F. Kapteijn and J. A. Moulijn, *Catal. Commun.*, 2005, **6**, 301–305.

101 G. Giecko, T. Borowiecki, W. Gac and J. Kruk, *Catal. Today*, 2008, **137**, 403–409.

102 S. Alini, F. Basile, S. Blasioli, C. Rinaldi and A. Vaccari, *Appl. Catal., B*, 2007, **70**, 323–329.

103 X. Wu, J. Du, Y. Gao, H. Wang, C. Zhang, R. Zhang, H. He, G. Lu and Z. Wu, *Chem. Soc. Rev.*, 2024, **53**, 8379–8423.

104 T. Nobukawa, M. Yoshida, K. Okumura, K. Tomishige and K. Kunimori, *J. Catal.*, 2005, **229**, 374–388.

105 M. Kögel, R. Mönnig, W. Schwieger, A. Tissler and T. Turek, *J. Catal.*, 1999, **182**, 470–478.

106 R. W. van den Brink, S. Booneveld, J. R. Pels, D. F. Bakker and M. J. F. M. Verhaak, *Appl. Catal., B*, 2001, **32**, 73–81.
107 M. A. G. Hevia and J. Pérez-Ramírez, *Environ. Sci. Technol.*, 2008, **42**, 8896–8900.
108 J. Pérez-Ramírez and F. Kapteijn, *Appl. Catal., B*, 2004, **47**, 177–187.
109 S. Du, B. Kang, X. Guo, Y. Wei, J. Jia and R. Zhang, *Catal. Lett.*, 2024, **154**, 3947–3957.
110 S. Roy, M. Hegde, S. Sharma, N. Lalla, A. Marimuthu and G. Madras, *Appl. Catal., B*, 2008, **84**, 341–350.
111 Y. Wu, X. Wu, J. Fan, H. Wang and Z. Wu, *Environ. Sci. Technol.*, 2024, **58**, 22583–22593.
112 L.-L. Zhang, X.-M. Chen and C.-G. Liu, *Inorg. Chem.*, 2019, **58**, 5221–5229.
113 Y. Qian, S. Yasumura, N. Zhang, A. Anzai, T. Toyao and K.-i. Shimizu, *Chin. J. Catal.*, 2025, **69**, 185–192.
114 J. W. A. Fischer, F. Buttignol, A. Garbujo, D. Ferri and G. Jeschke, *Chem. Sci.*, 2025, **16**, 4884–4891.
115 A. A. Khan, S. A. Alsalhi and A. U. Rahman, *Phys. Chem. Chem. Phys.*, 2024, **26**, 17110–17117.
116 A. H. Ragab, L. O. Mallasiy, S. R. Al-Mhyawi and I. Khan, *Diamond Relat. Mater.*, 2026, **161**, 113073.
117 M. Konsolakis, C. Drosou and I. V. Yentekakis, *Appl. Catal., B*, 2012, **123–124**, 405–413.
118 K. S. Chang, H.-J. Lee, Y.-S. Park and J.-W. Woo, *Appl. Catal., A*, 2006, **309**, 129–138.
119 J. H. Holles, M. A. Switzer and R. J. Davis, *J. Catal.*, 2000, **190**, 247–260.
120 T. Nobukawa, M. Yoshida, S. Kameoka, S.-i. Ito, K. Tomishige and K. Kunimori, *J. Phys. Chem. B*, 2004, **108**, 4071–4079.
121 B. R. Wood, J. A. Reimer, A. T. Bell, M. T. Janicke and K. C. Ott, *J. Catal.*, 2004, **225**, 300–306.
122 M. C. Campa, S. Morpurgo, G. Luccisano, M. Leone and D. Pietrogiacomi, *Microporous Mesoporous Mater.*, 2025, **398**, 113818.
123 M. C. Campa, D. Pietrogiacomi, C. Catracchia, S. Morpurgo, J. Olszowka, K. Mlekodaj, M. Lemishka, J. Dedecek, A. Kornas and E. Tabor, *Appl. Catal., B*, 2024, **342**, 123360.
124 S. Liu, S. Yasumura, Z. Maeno, T. Ohnishi and M. Ogura, *Appl. Catal., B*, 2025, **373**, 125365.
125 D. Pietrogiacomi, M. C. Campa, L. R. Carbone and M. Occhiuzzi, *Appl. Catal., B*, 2019, **240**, 19–29.
126 T. J. Vulic, A. F. K. Reitzmann and K. Lázár, *Chem. Eng. J.*, 2012, **207–208**, 913–922.
127 B. Guan, Z. Zhuang, L. Zhu, L. Xu, S. Chang, J. Ma, R. Wang, D. Yang, T. Zhu, H. Qu, B. Tan and Z. Huang, *Catal. Lett.*, 2026, **156**, 72.
128 B. Guan, Z. Zhuang, L. Zhu, X. Hu, C. Zhu, S. Zhao, J. Chen, J. Gao, K. Shu, H. Dang, L. Zhang, T. Zhu, Y. Li, L. Xu, W. Zeng, S. Chen, L. Wang, C. Zhu, J. He, Q. Xian and Z. Huang, *Fuel*, 2026, **406**, 136937.
129 J. W. Fischer, D. C. Cano-Blanco, H. Karas, F. Buttignol, O. Kröcher, D. Ferri and G. Jeschke, *ChemCatChem*, 2026, **18**, e01575.
130 Z. Zhuang, B. Guan, L. Zhu, X. Hu, C. Zhu, S. Zhao, J. Chen, K. Shu, H. Dang, J. Gao, L. Zhang, T. Zhu, M. Qian, W. Zeng, S. Chen, L. Wang, C. Zhu, J. He, Q. Xian and Z. Huang, *Chem. Eng. J.*, 2025, **522**, 167265.
131 J. H. Baek, S. M. Lee, J. H. Park, J. M. Jeong, R. H. Hwang, C. H. Ko, S. G. Jeon, T. H. Choi and K. B. Yi, *J. Ind. Eng. Chem.*, 2017, **48**, 194–201.
132 C.-G. Liu, Y.-J. Chu, L.-L. Zhang, C. Sun and J.-Y. Shi, *Environ. Sci. Technol.*, 2019, **53**, 12893–12903.
133 X. Zhang, Q. Shen, C. He, C. Ma, J. Cheng and Z. Hao, *Catal. Commun.*, 2012, **18**, 151–155.
134 L. Han, S. Cai, M. Gao, J.-y. Hasegawa, P. Wang, J. Zhang, L. Shi and D. Zhang, *Chem. Rev.*, 2019, **119**, 10916–10976.
135 Z. Zhang, Z. He, Y. Ye, Y. Wang, C. Liu, Y. Tan, Z. Yin and M. Pan, *Fuel Process. Technol.*, 2026, **284**, 108412.
136 X. Wang, Y. Xiong, H. Tan, Y. Liu, Y. Niu and T. Xu, *Energy Fuels*, 2012, **26**, 3125–3131.
137 W. Xie, Z. Sun, Y. Xiong, L. Li, T. Wu and D. Liang, *Int. J. Min. Sci. Technol.*, 2014, **24**, 471–475.
138 Z. Wang, H. Kuang, J. Zhang, L. Chu and Y. Ji, *Appl. Sci.*, 2019, **9**, 1656.
139 Z. Zhang, W. Zhong, C. Mao, Y. Xu, K. Lu, Y. Ye, W. Guan, M. Pan and D. Tan, *Energy*, 2024, **294**, 130899.
140 M. Zheng and X. Zhang, *Prog. React. Kinet. Mech.*, 2025, **50**, e003.
141 J. Sun, L. Li, G. Zhou, X. Wang, L. Zhang, Y. Liu, J. Yang, X. Lü and F. Jiang, *Environ. Sci. Technol.*, 2018, **52**, 4754–4762.
142 X. Lü, H. Li, X. Du, X. Wang, M. Lan, J. Wu, J. Zhu, J. Sun and F. Jiang, *React. Chem. Eng.*, 2020, **5**, 561–569.
143 W. Yang, Q. Zhao, H. Lu, Z. Ding, L. Meng and G.-H. Chen, *Water Res.*, 2016, **90**, 176–184.
144 J. T. Gleaves, G. Yablonsky, X. Zheng, R. Fushimi and P. L. Mills, *J. Mol. Catal. A: Chem.*, 2010, **315**, 108–134.
145 R. Fushimi and J. Gleaves, *Curr. Opin. Chem. Eng.*, 2018, **21**, 10–21.
146 R. Fushimi, in *Springer Handbook of Advanced Catalyst Characterization*, ed. I. E. Wachs and M. A. Bañares, Springer International Publishing, Cham, 2023, pp. 899–934, DOI: 10.1007/978-3-031-07125-6_40.
147 K. Morgan, N. Maguire, R. Fushimi, J. T. Gleaves, A. Goguet, M. P. Harold, E. V. Kondratenko, U. Menon, Y. Schuurman and G. S. Yablonsky, *Catal. Sci. Technol.*, 2017, **7**, 2416–2439.
148 E. V. Kondratenko and J. Pérez-Ramírez, *Catal. Today*, 2007, **119**, 243–246.
149 E. V. Kondratenko and J. Pérez-Ramírez, *Catal. Today*, 2007, **121**, 197–203.
150 E. V. Kondratenko and J. Pérez-Ramírez, *J. Phys. Chem. B*, 2006, **110**, 22586–22595.
151 E. V. Kondratenko, V. A. Kondratenko, M. Santiago and J. Pérez-Ramírez, *J. Catal.*, 2008, **256**, 248–258.
152 E. V. Kondratenko, V. A. Kondratenko, M. Santiago and J. Pérez-Ramírez, *Appl. Catal., B*, 2010, **99**, 66–73.
153 J. Pérez-Ramírez, F. Kapteijn, G. Mul and J. A. Moulijn, *J. Catal.*, 2002, **208**, 211–223.

154 V. Gölden, S. Sokolov, V. A. Kondratenko and E. V. Kondratenko, *Appl. Catal., B*, 2010, **101**, 130–136.

155 E. V. Kondratenko and J. Pérez-Ramírez, *Catal. Lett.*, 2003, **91**, 211–216.

156 E. V. Kondratenko and J. Pérez-Ramírez, *Appl. Catal., A*, 2004, **267**, 181–189.

157 V. A. Kondratenko and M. Baerns, *J. Catal.*, 2004, **225**, 37–44.

158 J. Pérez-Ramírez, E. V. Kondratenko and M. N. Debbagh, *J. Catal.*, 2005, **233**, 442–452.

159 E. V. Kondratenko and J. Pérez-Ramírez, *Appl. Catal., B*, 2006, **64**, 35–41.

160 V. Butera, *Phys. Chem. Chem. Phys.*, 2024, **26**, 7950–7970.

161 G. Henkelman, A. Arnaldsson and H. Jónsson, *Comput. Mater. Sci.*, 2006, **36**, 354–360.

162 B. Hammer and J. K. Norskov, *Nature*, 1995, **376**, 238–240.

163 K. Kim, S. Baek, J. J. Kim and J. W. Han, *Appl. Surf. Sci.*, 2020, **510**, 145349.

164 J. Sun, L. Wang, L. Zhang, Y. Zhao, Y. Chi, H. Wang, C. Li, J. Liu and J. Liu, *ACS Appl. Energy Mater.*, 2021, **4**, 8496–8505.

165 X. Wang, R. Duan, Z. Li, M. Gao, Y. Fu, Y. Han, G. He and H. He, *Environ. Sci. Technol.*, 2025, **59**, 5839–5847.

166 A. Heyden, B. Peters, A. T. Bell and F. J. Keil, *J. Phys. Chem. B*, 2005, **109**, 1857–1873.

167 A. Heyden, N. Hansen, A. T. Bell and F. J. Keil, *J. Phys. Chem. B*, 2006, **110**, 17096–17114.

168 K. McCullough, T. Williams, K. Mingle, P. Jamshidi and J. Lauterbach, *Phys. Chem. Chem. Phys.*, 2020, **22**, 11174–11196.

169 R. J. Hendershot, C. M. Snively and J. Lauterbach, *Chem. – Eur. J.*, 2005, **11**, 806–814.

170 R. Jayarathna, T. Onsree, S. Drummond, J. Naglic and J. Lauterbach, *J. Mater. Chem. A*, 2024, **12**, 3046–3060.

171 J. Hattrick-Simpers, C. Wen and J. Lauterbach, *Catal. Lett.*, 2015, **145**, 290–298.

172 T. N. Nguyen, T. T. P. Nhat, T. T. Phuong, K. Takimoto, A. Thakur, S. Nishimura, J. Ohyama, I. Miyazato, L. Takahashi, J. Fujima, K. Takahashi and T. Taniike, *ACS Catal.*, 2020, **10**, 921–932.

173 C. Kiener, M. Kurtz, H. Wilmer, C. Hoffmann, H.-W. Schmidt, J.-D. Grunwaldt, M. Muhler and F. Schüth, *J. Catal.*, 2002, **216**, 110–119.

174 R. J. Hendershot, R. Vijay, C. M. Snively and J. Lauterbach, *Chem. Eng. Sci.*, 2006, **61**, 3907–3916.

175 B. MacQueen, R. Jayarathna and J. Lauterbach, *Curr. Opin. Chem. Eng.*, 2022, **36**, 100781.

176 R. J. Hendershot, W. B. Rogers, C. M. Snively, B. A. Ogunnaike and J. Lauterbach, *Catal. Today*, 2004, **98**, 375–385.

177 J. Lyu, X. Liu, X. Ping, Q. Yang, S. Huang, X. Cao, X. Jia, N. Zhang, C. Huang and B. Wang, *J. Water Process Eng.*, 2025, **71**, 107306.

178 P. R. Adler, H. Nguyen, B. M. Rau and C. J. Dell, *Environ. Res. Commun.*, 2024, **6**, 091004.

179 H. Mashhadimoslem and A. Ghaemi, *Environ. Sci. Pollut. Res.*, 2023, **30**, 4166–4186.

180 C. Chen and S. P. Ong, *Nat. Comput. Sci.*, 2022, **2**, 718–728.

181 G. Olajide, K. Baral, S. Ezendu, A. Soyemi and T. Szilvasi, *J. Catal.*, 2025, **448**, 116202.

182 S. Ma, S.-D. Huang and Z.-P. Liu, *Nat. Catal.*, 2019, **2**, 671–677.

183 Y. Li, X. Duan, Z. Liu, C. Li, F. Ye, Z. Zhang, L. Chen, C. Du, Q. Wang and B. Shan, *Catal. Sci. Technol.*, 2024, **14**, 6286–6297.

184 H. Wang, Q. Wang, J. Zhao, C. Liu, J. Feng, J. Jin and D. Liu, *Mol. Catal.*, 2025, **584**, 115296.

185 G. Grzybek, J. Gryboś, P. Indyka, J. Janas, K. Ciura, B. Leszczyński, F. Zasada, A. Kotarba and Z. Sojka, *Appl. Catal., B*, 2021, **297**, 120435.

186 C. Zhang, Z. Zhang, C. Sui, F. Yuan, X. Niu and Y. Zhu, *ChemCatChem*, 2016, **8**, 2155–2164.

187 H. Yu, X. Wang and X. Wu, *Mol. Catal.*, 2018, **460**, 69–73.